Astrocytes expressing M_4 muscarinic acetylcholine receptor regulate locomotion and survival in murine prion disease

Gonzalo S. Tejeda[1*], Colin Molloy[1], Carrie K. Jones[2], Craig W. Lindsley[2], Graeme Milligan[1] and Andrew B. Tobin[1*]

[1] Centre for Translational Pharmacology, School of Molecular Biosciences, Advanced Research Centre, 11 Chapel Lane, University of Glasgow, Glasgow G11 6EW, Scotland, United Kingdom.

[2] Warren Centre for Neuroscience Drug Discovery, Department of Pharmacology, Innovation Park, 393 Nichol Mills Road, Franklin, Tennessee, 37027, USA.

[*]Corresponding authors:

Gonzalo.Tejeda@glasgow.ac.uk

Andrew.Tobin@glasgow.ac.uk

Abstract

Whilst there has been much focus on neuronally expressed muscarinic acetylcholine receptors (mAChRs), less attention has been paid to their expression and role in non-neuronal brain cells. Using genetically engineered mice, we identify a previously unappreciated subpopulation of astrocytes expressing the M4 mAChR subtype dispersed across various regions that include the brainstem, hypothalamus and, most abundantly, the cerebellum. Signalling and proteomic analysis of M4 mAChR positive astrocytes from the cerebellum confirmed functional receptor expression and its role in

regulating protein expression. Genetic ablation of these astrocytes in mice revealed a specific role in locomotion. Importantly, in the context of murine prion disease, we observed a significant expansion of M4 mAChR positive astrocytes, and ablation experiments established that this astrocyte subpopulation has a detrimental effect on late-stage disease. Together we identify M4 mAChR expressing astrocyte subpopulation that plays a specific role in normal neurophysiology and the progression of inflammatory neurodegenerative disease.

Keywords: Astrocyte, M_4 muscarinic acetylcholine receptor, G protein-coupled receptor, neuroinflammation, locomotion.

Main Text

Background

The muscarinic acetylcholine receptors (mAChRs) have been under intense investigation due to the critical role of this family of G protein-coupled receptors (GPCRs) in the regulation of various neuronal processes, including learning, memory, reward and seek behaviour. Among the five subtypes (M_1-M_5 mAChRs), M_1 and M_4 have emerged as particularly important in brain function and they are considered promising therapeutic targets for the treatment of several brain disorders (1, 2). However, while most research on mAChRs in the central nervous system (CNS) has focused on neuronal expression and function, much less is known about their roles in non-neuronal cells.

46 Some of the strongest evidence for mAChRs function in glial cells comes from studies
47 on M_1 mAChR in oligodendrocyte precursor cells (OPCs), where specific ablation of this
48 receptor gene enhances remyelination in mouse models of autoimmune
49 encephalomyelitis (3), hypoxia (4), aging (5) and Alzheimer's disease (6). Additional
50 clues suggest that mAChRs may regulate neuroinflammation. For example, our studies
51 in a prion model of neurodegeneration (7), and others in mouse models of Alzheimer's
52 disease (8), have shown that the activation of the M_1 mAChR by selective positive
53 allosteric modulators (PAMs) reduced markers of astrocyte and microglial activation.
54 However, whilst transcripts for the mAChR family have been reported in astrocytes and
55 microglia (9, 10), including the M_4 mAChR (11-13), little is known about the
56 contribution that these receptors play in the regulation of glial cells.

57 Here, we used a transgenic mouse model expressing CRE recombinase under the
58 control of the M_4 mAChR gene promoter (*Chrm4*) to discover a discrete population of
59 M_4 mAChR-expressing astrocytes located in the brainstem, hypothalamus, and
60 cerebellum. Signalling and proteomic studies confirmed the functional expression of
61 this receptor subtype in astrocytes, particularly within the cerebellum. CRE-mediated
62 deletion of M_4 mAChR expressing astrocytes exposed the role of this subpopulation of
63 astrocytes in locomotion. Importantly, our study unveiled the expansion of the M_4
64 mAChR expressing astrocytes in parallel with the progression of prion
65 neurodegenerative disease. Genetic ablation of these astrocytes significantly extended
66 the lifespan of prion-diseased mice, suggesting a detrimental role in disease
67 progression. Together our data point to a previously unappreciated subpopulation of
68 M_4 mAChR expressing astrocytes that play a specific role in normal neurophysiology
69 and inflammatory neurodegenerative disease.

70 ## Results

71 ### Generation of a genetic mouse model to identify M_4 mAChR expressing cells

72 To facilitate the study of the diversity and distribution of M_4 mAChR expressing cells
73 (M_4^+ cells) in the brain, we generated a mouse line that expresses a CRE recombinase
74 under the control of the *Chrm4*-promoter (Chrm4-CRE-IRES-mM4, hereinafter referred
75 to as $Chrm4^{CRE}$) **(Fig. 1a)**. In these mice, the *Chrm4* locus was modified to contain an
76 internal ribosomal entry site (IRES) cassette followed by the CRE recombinase coding
77 sequence down-stream of the M_4 mAChR receptor exon 3 **(Fig. 1a)**. By crossing these
78 mice with a CRE-dependent green fluorescent protein (GFP) reporter mouse strain
79 (R26-CAG-GFP,-MetRS^{*L274G}, also called R26-MetRS*), we aimed to generate animals
80 where the GFP acts as a marker of M_4 mAChR expressing cells (14) **(Fig. 1a)**. The
81 resulting mouse strain ($Chrm4^{CRE}$::MetRS*), heterozygous for both alleles, showed
82 similar levels of M_4 mAChR expression to that of wild-type mice as determined by
83 radio-ligand binding experiments of striatal membranes **(Supplementary Fig. 1a)**.
84 Examination of brain sections of $Chrm4^{CRE}$::MetRS* animals revealed GFP-positive
85 neurons (stained with the neuronal marker MAP2) especially abundant in the striatum,
86 cortex, and hippocampus **(Fig. 1b)**, areas where Western blots confirmed M_4 mAChR
87 expression **(Supplementary Fig. 1b)** consistent with previous studies (15-18). These
88 experiments, together with the lack of GFP signal detected in the brain of the parental
89 lines **(Supplementary Fig. 1c)**, give confidence that the reporter-GFP system acts as a
90 surrogate marker for M_4 mAChR expressing cells/neurons.

91 ### M_4 mAChRs expression in a discrete astrocytic subpopulation

92 In addition to M_4^+ neurons, we also detected dispersed populations of M_4^+ stellate cells
93 in the midbrain, hypothalamus, and the pons **(Fig. 1c)**. These cells did not co-localise
94 with markers for microglia, oligodendrocytes or neurons **(Supplementary Fig. 1d)** but
95 rather co-stained with antibody markers for glial fibrillary acidic protein (GFAP) and
96 S100β, thereby identifying them as M_4^+ astrocytes **(Fig. 1c, Supplementary Fig. 1e)**.

97 These experiments also revealed a surprisingly diverse array of M_4^+ cells in the
98 cerebellum **(Fig. 2a),** a region with low but detectable levels of M_4 mAChR transcript
99 **(Supplementary Fig. 2a)**. In contrast, no significant GFP staining was observed in the
100 cerebellum of the parental mouse strains **(Supplementary Fig. 2b)**. Among these M_4^+
101 cells, we could identify a sparse population of M_4^+ Purkinje neurons, labelled with the
102 calcium-binding protein calbindin D-28k **(Fig. 2b)**. Most strikingly, however, was the
103 abundance of cerebellum M_4^+ cells that co-stained with astrocytic markers (GFAP,
104 NDRG2, S100β) **(Fig. 2c, Supplementary Fig. 2c)**. The location and morphology of these
105 cells indicated that they correspond to Bergmann glia in the Purkinje layer, some velate
106 astrocytes in the granule cell layer, dispersed fibrous astrocytes surrounding the white
107 matter and a large population of M_4^+ astrocytes within the cerebellar nuclei **(Fig. 2c).**

108 **Signalling analysis of astrocyte M_4 mAChRs**

109 To determine the functional expression of M_4 mAChRs in glial cells, primary astrocyte
110 cultures were prepared from the cerebrum and the cerebellum of Chrm4^{CRE}::MetRS*
111 mice. In line with the observations in intact brain, M_4^+ astrocytes represented only a
112 small proportion of the total astrocyte population prepared from the cerebrum (8.7 ±
113 2.4 %), whilst a higher proportion (30.4 ± 3.8 %) of M_4^+ astrocytes were evident in
114 cerebellar cultures **(Fig. 3a, b)**.

115 To establish if these M_4^+ astrocytes expressed functional M_4 mAChRs, we took
116 advantage of previous studies that showed that muscarinic agonists can induce
117 accumulation of the Immediate Early-Gene (IEG) c-fos in cultured astrocytes (19).
118 Therefore, we treated cerebellar astrocytes prepared from $Chrm4^{CRE}$::MetRS* mice
119 with the muscarinic agonist oxotremorine (10 µM). This resulted in a significant up-
120 regulation of c-fos expression in M_4^+ astrocytes **(Fig. 3c, d)**. Furthermore, preincubation
121 with VU0467154 (VU154, 10 µM), a M_4 mAChR PAM (20), increased the number of
122 oxotremorine-induced c-fos$^+$ cells in the cerebellar astrocyte cultures, whilst
123 pretreatment with the highly selective M_4 mAChR antagonist VU6028418 (VU418, 5
124 µM) (21) prevented oxotremorine-induced stimulation of c-fos in these cells **(Fig. 3c,**
125 **d)**. Additionally, we probed the phosphorylation of the extracellular signal-regulated
126 kinases 1/2 ($pERK_{1/2}$), a signalling pathway downstream of M_4 mAChR-Gi activation.
127 Treatment with oxotremorine increased $pERK_{1/2}$ levels in a concentration-dependent
128 manner (pEC_{50} = 5.57 ± 0.21, **Supplementary Fig. 3a**) whereas the M_4 mAChR
129 antagonist VU418 (1 µM) shifted the curve to higher agonist concentrations (pEC_{50} =
130 4.61 ± 0.22, p = 0.002) consistent with VU418 selective antagonism of the M_4 mAChR
131 $ERK_{1/2}$ response.

132 **Proteomic evaluation of astrocyte M_4 mAChRs**

133 To further characterise the functional M_4 mAChR response in cerebellar astrocytes, we
134 analysed changes in *de novo* synthesised proteins in response to receptor activation. In
135 these experiments we took advantage of the fact that, in addition to the expression of
136 GFP, the $Chrm4^{CRE}$::MetRS* mice contain a mutated methionyl-tRNA synthetase (MetRS
137 L274G) expressed in a CRE-dependent manner. The enlarged binding pocket of this

138 mutant synthetase allows for the incorporation of the unnatural amino acid
139 azidonorleucine (ANL) into nascent proteins, which can later be tagged by click
140 chemistry for identification of labelled proteins or for biochemical purification (14).
141 Since our system results in CRE-expression only in M_4^+ cells (i.e. astrocytes) then the
142 mutated methionyl-tRNA synthetase will only be expressed in M_4^+ astrocytes. In this
143 way, although our cerebellar astrocyte cultures are mixed (~30% of the astrocytes are
144 M_4^+ **(Fig. 3b)**), we could conduct proteomic analysis on proteins synthesised exclusively
145 in M_4^+ astrocytes.

146 We first tested our system by exposing cerebellar astrocyte cultures, prepared from
147 Chrm4^{CRE}::MetRS* mice, to ANL (4 mM) followed by fixation, permeabilization and
148 labelling ANL-incorporated proteins with the fluorescent Cy3-alkyne tag – process
149 referred to as fluorescent non-canonical amino acid tagging (FUNCAT). This established
150 a FUNCAT signal (Cy3) that was restricted to M_4^+ astrocytes (identified by GFP and
151 S100β) **(Supplementary Fig. 3b)**.

152 Next, we collected lysates from ANL treated cerebellar astrocytes prepared from
153 Chrm4^{CRE}::MetRS* mice and using click chemistry incorporated a biotin-tag to ANL
154 incorporated proteins. Western blot analysis revealed an abundance of biotinylated
155 nascent proteins using this approach **(Supplementary Fig. 3c)**. These biotinylated
156 proteins were purified using avidin beads and proteins identified by mass spectrometry
157 **(Supplementary Data 1)**. These experiments detected a total of 260 enriched
158 biotinylated proteins **(Fig. 3e)**. A gene ontology (GO) analysis revealed enrichment of
159 astrocytic markers (GFAP, vimentin, 3-phosphoglycerate dehydrogenase), confirming
160 the specific labelling. Importantly, terms associated with metabolic enzymes,

161 translation and cytoskeleton components were among the most significantly enriched
162 GO groups **(Fig. 3f)**. Furthermore, oxotremorine (10 μM) treatment induced the
163 synthesis of 67 unique proteins that were dependent on M_4 mAChR activation, as they
164 were not identified in the presence of the specific M_4 mAChR antagonist (VU418, 5
165 μM). A GO enrichment analysis showed that proteins up-regulated by M_4 mAChR
166 activation are involved in trafficking and protein translation **(Fig. 3g)**, including the
167 actin-binding profilin-2, the metallothionein subtypes II (MT2) and III (MT3), guanylate-
168 binding protein 2 (GBP2), and the MAP kinase ERK_2.

169 **Diptheria toxin-mediated ablation of M_4^+ astrocytes effects locomotion**

170 In order to decipher the role of M_4^+ astrocytes, we followed a genetic strategy of
171 targeted ablation. The mouse strain Aldh1l1-eGFP,-DTA (22), expresses eGFP in
172 astrocytes and a CRE-dependent diphteria toxin A (DTA). Crossing these animals with
173 the Chrm*4*^{CRE} strain results in a mouse (Chrm4^{CRE}:: Aldh1l1^{DTA}) where M_4^+ astrocytes are
174 selectively ablated **(Fig. 4a)**. As M_4 mAChR expression was observed in some
175 hypothalamic astrocytes **(Fig. 1b)**, we first evaluated the body weight of these animals
176 over time and found no differences compared to wild type littermates **(Fig. 4b)**. Also,
177 these animals showed similar food consumption and organ weights **(Supplementary**
178 **Fig. 4a, b)**. Previous studies have indicated that alterations in cerebellar astrocytes,
179 specifically Bergmann glia, led to cerebellar atrophy and motor impairment (23).
180 However, we did not observe any abnormalities in the morphology or the overall glial
181 composition of the cerebellum of the Chrm*4*^{CRE}:: Aldh1l1^{DTA} animals when compared to
182 the cerebellum of the parental line **(Supplementary Fig. 4c)**. Furthermore, the
183 Chrm4^{CRE}:: Aldh1l1^{DTA} mice did not show ataxia or any deficits in motor coordination as

184 determined by the hindlimb clasping, ledge and rotarod tests **(Fig. 4c)**. In contrast,
185 exploratory behaviour evaluated in an open field test showed that Chrm4^{CRE}::
186 Aldh1l1^{DTA} mice exhibited significantly increased time in the centre of the arena
187 compared to littermate controls (74.1 ± 6.7 and 51.4 ± 2.6 s, respectively, $p < 0.01$, **Fig.**
188 **4d**), while the overall locomotion was reduced (24.1 ± 1.5 m travelled in the arena
189 versus 30.6 ± 1.7 m for control mice) and the time spent immobile (231.0 ± 13.7 s) was
190 greater than wild type littermates (164.7 ± 14.4 s) **(Fig. 4e, Supplementary Fig. 4d)**.
191 These results could be interpreted as deficits in anxiety-like behaviour, but a further
192 evaluation in an elevated plus maze test excluded this possibility, as Chrm4^{CRE}::
193 Aldh1l1^{DTA} mice performed similarly to wild type littermates in this paradigm **(Fig. 4e,**
194 **Supplementary Fig. 4e)**.

195 These data suggest a potential role for M_4^+ astrocytes in locomotion which was tested
196 further by implant telemetry. Both Chrm4^{CRE}:: Aldh1l1^{DTA} and wild type littermate mice
197 had peaks of activity at similar times and of similar duration, excluding the possibility of
198 disturbed sleep **(Fig. 4g)**. Moreover, fluctuations in body temperature followed a
199 similar pattern, with no differences observed between the two groups of animals
200 **(Supplementary Fig. 4f)**. Interestingly, when considering the overall activity in each
201 phase, it was evident that Chrm4^{CRE}:: Aldh1l1^{DTA} mice moved less intensely during the
202 dark phase (7.85 ± 0.61 counts) than their control littermates (9.93 ± 0.95 counts) **(Fig.**
203 **4h)**. These findings are consistent with a deficit in the overall locomotor activity when
204 the M_4^+ astrocytes are ablated.

205 **M_4^+ astrocytes do not regulate amphetamine hyperlocomotion**

206 M_4 mAChRs are known to counteract hyperlocomotion induced by amphetamine or the
207 glutamate receptor agonist MK-801 (20, 24). This pivotal function in motor behaviours
208 has been attributed to neuronal (presynaptic) M_4 mAChR regulation of the dopamine
209 release and signalling in the basal ganglia (25-28). Here, we examined if M_4^+ astrocytes
210 might contribute to this by testing the efficacy of a M_4 mAChR selective PAM, VU154,
211 to reverse amphetamine-induced hyperlocomotion in Chrm4^{CRE}:: Aldh1l1^{DTA} and
212 littermate control mice. Administration of VU154 (10 mg/kg, i.p.) 20 mins before
213 amphetamine (2 mg/kg, i.p.) significantly decreased amphetamine-induced
214 hyperlocomotion in both groups of mice **(Fig. 4i, j)**. Likewise, both genotypes displayed
215 comparable measurements in mobility time **(Supplementary Fig. 4g)**. Together these
216 data indicate that the role of M_4^+ astrocytes in locomotion observed earlier is
217 independent from the dopamine-dependent motor function of M_4 mAChR in the basal
218 ganglia.

219 **M_4^+ astrocytes during prion disease**

220 There is currently intense interest in the role of astrocytes in regulating the onset and
221 progression of many neurodegenerative diseases and other brain disorders (29, 30). It
222 is clear, however, that the responses to pathological stimuli of reactive astrocytes are
223 very diverse, which could reflect the heterogeneous nature of astrocyte
224 subpopulations with established differences in origin and temporal function (31). Here
225 we probed the potential involvement of M_4^+ astrocytes in the pathology of murine
226 prion disease, a progressive terminal neurodegenerative disease model associated with
227 pronounced neuroinflammation and astrogliosis (32). Prion disease was induced in
228 Chrm4^{CRE}::MetRS* mice by inoculation with Rocky Mountain Laboratory (RML) prion-

229 infected brain homogenate. At 20 weeks post-inoculation (w.p.i.), a sharp increase was
230 observed in the number of M_4^+ astrocytes **(Fig. 5a)**, as determined by co-staining with
231 the astrocytic marker GFAP **(Supplementary Fig. 5a)**. The lack of co-staining of these
232 M_4^+ cells with microglial marker Iba1 excluded the possibility that these cells were
233 infiltrating macrophages **(Supplementary Fig. 5b)**. In fact, the strong GFAP staining is
234 consistent with these M_4^+ cells showing characteristics of reactive astrocytes, which
235 was particularly evident in the region of the cerebellar nuclei **(Fig. 5b)**.

236 A rostro-caudal examination of serial brain sections from RML-inoculated
237 Chrm4^{CRE}::MetRS* mice demonstrated that M_4^+ astrocytes were profoundly up-
238 regulated in disease, even in regions such as the cortex, the hippocampus and the
239 thalamus where these cells were not evident under normal "non-disease" conditions
240 **(Supplementary Fig. 5a, b, c)**. To interrogate regional differences, we estimated the
241 number of M_4^+ astrocytes in each area during prion disease and displayed the cellular
242 densities as heat maps overlaid onto the brain anatomy **(Fig. 5c)**. Our results indicated
243 that the hypothalamus hosts the largest number of M_4^+ astrocytes. As prion disease is
244 rapidly progressive, we further studied the evolution of these cellular subpopulations
245 by comparing three time points after RML-inoculation (15, 18 and 23 w.p.i., **Fig. 5c,**
246 **Supplementary Fig. 5d)**. We found that the number of M_4^+ reactive astrocytes
247 gradually increased in almost all examined brain regions over time **(Fig. 5d)**.
248 Interestingly, this prion-induced expansion was not observed in one of the biggest
249 reservoirs of M_4^+ astrocytes, the cerebellar nuclei within the arbor vitae
250 **(Supplementary Fig. 5e)**, although astrocytes in this region showed a prominent
251 reactivity during disease **(Fig. 5b)**. Critically, M_4^+ astrocytes showed expression of GBP2
252 during prion disease **(Fig. 5e)**, a marker associated with a neurotoxic or pro-

253 inflammatory phenotype (33). In addition to GBP2, these astrocytes also expressed
254 metallothionein III (MT3) **(Supplementary Fig. 5f)**, which was similarly identified in our
255 proteomic analysis as being upregulated upon activation of the M4 mAChR
256 **(Supplementary Data 1)**. This spatio-temporal analysis of the M_4^+ astrocytes in prion
257 disease indicated that these cells become activated in a pathological context and the
258 number of reactive astrocytes that express the M_4 mAChR continuously increases
259 alongside the progression of the disease.

260 **Increased lifespan of prion disease inoculated mice where M_4^+ astrocytes are ablated**

261 To establish the potential role played by M_4^+ astrocytes in prion disease, we evaluated
262 the disease progression in mice where the M_4^+ astrocytes had been ablated.
263 Inoculation of both Chrm4^{CRE}:: Aldh1l1^{DTA} and wild type littermate mice with RML
264 resulted in a similar onset of prion disease and early/mid disease progression, as
265 determined by near equivalent times when at least two early "clinical" signs of prion
266 disease appeared **(Supplementary Fig. 6a)**. Similarly, there was equivalence in
267 progressive weight loss **(Supplementary Fig. 6b)**, decreased motor co-ordination and
268 decline in burrowing behaviour (a sign of hippocampal function) between the
269 genotypes **(Fig. 6a, b)**. Importantly, despite a similar progression of early and mid-
270 stages of disease, Chrm4^{CRE}:: Aldh1l1^{DTA} mice showed extended lifespan compared to
271 wild type littermates (mean survival 164.7 ± 0.9 and 158.6 ± 1.5 days, respectively, $^{**}p$
272 < 0.01) **(Fig. 6c).** This survival effect was more prominent in females **(Fig. 6d)**, which
273 could be explained by their shorter incubation periods to Prp^{Sc} compared to males **(Fig.
274 6e)** when exposed to the same quantity of infectious material (34). Our result
275 emphasises the importance of sex as a biological variable in prion pathogenesis,

276 previously observed in mice depleted of NG2 glia (35) and in human sporadic
277 Creutzfeldt-Jakob disease (sCJD) (36).

278 We next assessed the accumulation of misfolded, insoluble scrapie prion protein
279 (Prp^{Sc}), which constitutes the major component of infectious prion disease. At the
280 terminal stage, a dramatic deposition of Prp^{Sc} was detected in the hippocampus,
281 cortex, striatum and cerebellum of prion-inoculated mice when compared to the non-
282 diseased controls **(Fig. 6f, g)**. Importantly, the accumulation of Prp^{Sc} was significantly
283 decreased in prion inoculated $Chrm4^{CRE}$:: $Aldh1l1^{DTA}$ compared to wild type controls in
284 the cerebellum, but not in the rest of the brain regions **(Fig. 6g)**. However, this
285 reduction was not accompanied by changes in other indicators of neurodegeneration
286 (ApoE and serpinA3N) or markers of neuroinflammation (GFAP, Iba1 and clusterin)
287 **(Supplementary Fig. 6c, d)**. Overall, these data indicate that the ablation of M_4^+
288 astrocytes does not affect the onset of the clinical symptoms or progression of prion
289 disease but extends the lifespan of mice, indicating a potential detrimental effect of
290 M_4^+ astrocytes in the later stages of disease.

291 Discussion

292 Despite the considerable progress in understanding the neuronal populations that
293 display the M_4 mAChR (37-39), the identity, location and function of non-neuronal CNS
294 cells, in particular glial cells, expressing this receptor subtype have remained largely
295 unexplored. Here, we reveal a discrete subpopulation of M_4 mAChR expressing
296 astrocytes dispersed across several areas of the mouse CNS. Genetic ablation of these
297 astrocytes demonstrated a role in neurological responses associated with locomotion,
298 while other M_4 mAChR-associated processes such as anxiety and the regulation of

299 responses to amphetamine remained unaffected. Importantly, there was a dramatic
300 expansion of this subpopulation of astrocytes during the progression of
301 neurodegeneration in a model of prion disease. Ablation studies indicated a
302 detrimental role for these M_4^+ astrocytes in later disease stages. In these ways our
303 study contributes to a growing awareness that astrocytes are not uniform but rather a
304 diverse set of cell types with varying cellular and functional characteristics.
305 Appreciating the nature and complexity of the various subtypes of astrocytes will be
306 essential if we are to understand their role in normal neurophysiology and if we are to
307 target these cells in brain diseases.

308 Under physiological conditions, we found M_4^+ astrocytes in the hypothalamus and
309 dorsal parts of the brainstem. These regions are critical regulators of energy balance
310 and appetite, and astrocytes in these areas have been reported to contribute to these
311 tasks by modulating the activity of adjacent neurons (40). Thus, manipulation of
312 hypothalamic and brainstem astrocytes has been reported to influence metabolic
313 processes including feeding and glucose metabolism (41-46), as well as circadian
314 rhythm, and sleep (47, 48). Interestingly, ablation of M_4^+ astrocytes in mice did not
315 result in alterations in the weight, body temperature or daily activity cycle. It was,
316 however, of relevance that M_4^+ astrocytes regulate locomotion, an activity consistent
317 with the expression of the receptor in a diverse array of the cerebellar astrocytes,
318 which are activated during voluntary and enforced locomotion (49, 50). It is important
319 to note that M_4^+ astrocytes are involved in specific aspects of motor control whilst
320 other behaviours such as balance and coordination, typically altered after a loss of
321 Bergmann glia support (23), remained normal in M_4^+ astrocyte-depleted mice.
322 Furthermore, the ablation of M_4^+ astrocytes had no impact on basal ganglia-mediated

323 hyperlocomotion responses, classically linked with neuronal M_4 mAChRs (25-28),
324 despite the fact that astrocytes in this region can modulate these psychomotor
325 behavioural effects (51). Hence, our studies have dissected a locomotion response that
326 may be under the regulation of M_4 mAChR expressed on a subpopulation of astrocytes.

327 While our study primarily identified the existence of a novel population of astrocytes,
328 the neuro-anatomical distribution of these cells, and the function that these astrocytes
329 might play under normal and neurodegenerative disease scenarios, it is a particular
330 challenge to relate this to the activity of M_4 mAChRs themselves. We started to
331 investigate this in primary cultures where we used a genetic approach that allows for
332 the signalling and proteomic interrogation of the M_4^+ cerebellar astrocytes amongst a
333 mixed population of astrocytes. This has provided an in-depth proteomic profile of M_4^+
334 astrocyte subpopulation and demonstrated that selective M_4 mAChR activation
335 resulted in the regulation of key cytoskeletal, metabolic and translational proteins that
336 can significantly impact astrocyte biology and activation status. For example, profilin-2
337 can modulate astrocytic morphology (52); MT3 plays a role in the clearance of the
338 prion-like amyloid β (53), and the low-density lipoprotein receptor-related protein-1
339 (LRP1) is important for the astrocyte-neuron communication (54, 55). Interestingly,
340 LRP1 is downregulated together with M_4 mAChR in the cerebellum of patients with
341 Rett syndrome (56), and mouse models show motor deficits when the *MeCP2* gene is
342 deleted from the cerebellum but not when is restricted to Purkinje or granular neurons
343 (57), highlighting the contribution of the cerebellar astrocyte pool.

344 The involvement of astrocytes, and indeed microglia, in protection against
345 neurodegenerative diseases is an extremely active area of research (58). Astrogliosis is

346 a widespread response in prion disease, although each brain region contains reactive
347 astrocytes with heterogenous phenotypes and functions determined by the
348 microenvironment (59). Our study showed a striking increase in M_4^+ astrocytes in the
349 thalamus and hypothalamus, brain regions identified as particularly susceptible to
350 prion deposition and neuroinflammatory cascades in RML and other prion strain
351 models (60, 61). Astrocytes are known to adopt either neuroprotective or neurotoxic
352 phenotypes in response to pathological stimuli. While their early activation may
353 support neuronal survival and clearance of misfolded proteins, functions that are
354 protective in diseases like Alzheimer's disease (62), the prolonged activation of
355 astrocytes is widely considered to be detrimental (63, 64). This certainly seems to be
356 the case for M_4^+ astrocytes which do not seem to make a significant impact on early-
357 and mid-stages of disease but rather are involved in acceleration of the later stages of
358 disease. The expression of GBP2 in M_4^+ astrocytes, a marker linked to neurotoxic
359 reactivity, further supports their detrimental role in late-stage disease. How the M_4
360 mAChR itself is involved in the regulation of these astrocytes at latter disease stages,
361 and whether agonists or antagonists might make an impact is at present uncertain.
362 What is clear, however, is that our findings support the selective targeting of neurotoxic
363 astrocytes while preserving glial subtypes with neuroprotective roles as a promising
364 therapeutic strategy for prion disease. A therapeutic option previously discarded after
365 observing that preventing the formation of the neurotoxic $C3^+$ astrocytes in mice
366 accelerated disease progression (33). This dichotomy highlights the delicate balance
367 between protective and harmful astrocyte states and the need for careful and
368 thorough characterisation of these astrocytic subpopulations.

369 In conclusion by identifying a previously unappreciated astrocyte subpopulation we not
370 only provide further evidence of the diversity of astrocytes but by ablation of M_4^+
371 astrocytes highlight the role of this astrocyte population in the regulation of
372 locomotion and neurodegenerative disease pathology.

373 ## Materials and Methods

374 ### Animals

375 Mice were maintained on a 12-h light–dark cycle with ad libitum standard mouse chow
376 food and water.

377 ### Generation of Chrm4^{CRE} mice

378 Transgenic Chrm4^{CRE} mice were generated by genOway (Lyon, France). Briefly, a CRE-
379 IRES cassette was inserted in frame of the ATG in exon 2 of the endogenous *Chrm4*
380 gene, by homologous recombination in embryonic stem (ES) cells. To this end a
381 targeting vector was created containing long and short homology arms to the *Chrm4*
382 genomic region. The targeted vector was completed with an FRT-flanked neomycin
383 resistance gene upstream the CRE sequence to select ES cells that had undergone
384 homologous recombination, and a diphtheria toxin cassette upstream the long
385 homology arm for negative selection. The linearised targeting construct was
386 transfected into C57BL/6N ES cells by electroporation. Positive clones were assessed by
387 PCR and whole locus sequence analysis to validate the presence of the correct
388 recombination event before being injected into blastocysts derived from C57BL/6J
389 female mice. The resulting highly chimeric males (chimerism rate above 50%) were
390 then crossed to a FLP recombinase-expressing deleter mouse strain to generate

391 heterozygous knock-in animals devoid of neomycin. Genotyping was initially confirmed
392 by PCR on genomic DNA obtained from ear biopsies using the primers 5'
393 CACTGCCCACCTGTCTCCAG and 5' GGTTGTGGGCTGTTGTGACCAG, which flank the
394 insertion site of the CRE-IRES cassette; and further confirmed with the pair of primers
395 5' GCTAGAGCCTGTTTTGCACG and 5' GCTAGAGCCTGTTTTGCACG, which amplify a
396 region of the CRE recombinase sequence. PCR-positive animals were further validated
397 by whole locus sequencing. The results were later corroborated by fluorescent
398 quantitative PCR (qPCR) using a commercial genotyping service (Transnetyx, Cordova,
399 TN). This service also analysed further samples to verify the genotype of the first litter
400 of every new breeder pair for the maintenance of the Chrm4^{CRE} colony.

401 Homozygous Chrm4^{CRE} were crossed with homozygous R26-CAG-GFP,-MetRS* (Jackson
402 Laboratory, strain: 028071) to generate Chrm4^{CRE}::MetRS*, and heterozygosity for both
403 alleles was confirmed by Transnetyx genotyping service. Chrm4^{CRE} animals were mated
404 with hemizygous Aldh1l1-eGFP,-DTA mice (Jackson Laboratory, strain: 026033) to
405 produce Chrm4^{CRE}::Aldh1l1^{WT} and Chrm4^{CRE}:: Aldh1l1^{DTA}. All these animals were
406 genotyped with specific probes designed for CRE recombinase, eGFP and Chrm4
407 sequences at weaning by a commercial vendor (Transnetyx). Chrm4^{CRE}:: Aldh1l1^{DTA} and
408 wild type littermate animals were kept mixed in housing cages, except when measuring
409 the food and water intake and during telemetry monitoring experiments. The
410 generation of M_4 KO mice has been described elsewhere (65).

411 **Measurement of organ weight, food and water consumption**

412 Chrm4^{CRE}:: Aldh1l1^{DTA} and wild type littermate mice were housed separated by
413 genotype and food and water intakes were measured every 3 days for 1-2 weeks.

414 Average daily food and water consumption per animal were calculated and no
415 differences were observed between genotypes or sex.

416 The brain, liver, heart, spleen and kidneys from Chrm4^{CRE}:: Aldh1l1^{DTA} and wild type
417 littermate animals were collected (n=3-5, 4-5 months old) and the weight was recorded
418 and adjusted for body weight. Organ dimensions were also measured, and no
419 differences were observed (data not shown).

420 **Rotarod**

421 Motor performance was tested using the 5-lane rotarod (Cat. #47650, Ugo Basile,
422 Germany). Mice were weighed prior every testing, which happened weekly for both
423 prion infected and non-infected 10-week-old male mice for 15-20 weeks. Each day,
424 mice were placed on the 3 cm diameter rod for 2 habituation phases, consisting of a
425 constant rotation speed at 4 rpm for 90 s. For the testing phase, the animals were
426 placed on the rod that accelerated from 4 rpm to 40 rpm over a period of 5 min. The
427 mice were tested 2 times with a rest period of at least 15 min between each trial.
428 Animals that fell before the rod reached 15 rpm speed were placed back on the beam,
429 but if they fell more than once in that period, they were returned to the home cage. If
430 mice turned on the rod, the test was stopped, and the time recorded. The latency to
431 fall (time that the mouse remains on the rod) was registered automatically by a trip
432 switch under the floor of each rotating drum, and the result was used as an indicator of
433 motor coordination. The activity of Chrm4^{CRE}:: Aldh1l1^{WT} in this test was comparable to
434 wild type animals with a C57BL/6 background (data not shown).

435 **Elevated Plus Maze (EPM)**

436 The EPM test was used to assess anxiety-related behaviour in mice. 9-10 weeks old
437 male and female animals were placed in the centre of a cross shaped maze (arms of 50
438 x 10 cm), with 2 enclosed arms (black walls of 30 cm height) and 2 dimly illuminated
439 open arms opposite each other. The test was performed before the start of the light
440 cycle and lasted for 5 min. The time spent in the open arms versus the enclosed spaces
441 versus, the immobility time and the number of entries to each arm were recorded
442 using the ANY-maze video tracking software (Stoelting).

443 **Open field**

444 The open field activity of 8-12 weeks old male and female mice was monitored using a
445 clear Perspex square box (50 × 50 cm). Animals were placed in the centre of the
446 illuminated open field arena and allowed to freely explore for 10 minutes. The time
447 spent in the centre of the arena, the distance travelled and speed were assessed using
448 the ANY-maze tracking system (Stoelting).

449 **Hindlimb clasping test**

450 The degree of hindlimb clasping as an indicator of motor dysfunction was evaluated in
451 8-9 weeks old mice. Animals were suspended by their tails for 10-20 s and rated from 0
452 to 3 according to the following score system: 0 corresponded to hindlimbs
453 consistently splayed outward and away from the abdomen; 1 was assigned when
454 one hindlimb was retracted inwards towards the abdomen for more than 50% of the
455 time; a score of 2 meant that both hindlimbs were partially retracted inwards towards
456 the abdomen for at least 50% the time; and 3 was given when both hindlimbs were
457 entirely retracted inwards towards the abdomen for at least 50% of the observation

458 period (66). Two separate trials were performed per animal. All evaluated Chrm4^{CRE}::
459 Aldh1l1^{DTA} and Chrm4^{CRE}:: Aldh1l1^{WT} animals showed a consistent score of 0 in this test.

460 **Ledge test**

461 Mice aged 8-9 weeks old were placed on the cage ledge and recorded to measure
462 balance and coordination. Paw placement and forward movement as it walked along
463 the ledge were observed and scored from 0 to 3 as in (66): 0, for normal walking; 1, if
464 the mouse lost its footing; 2, if the hindlimbs were not used, and 3, if the animal fell off
465 the ledge. Data from three trials were averaged for each mouse and none of the
466 Chrm4^{CRE}:: Aldh1l1^{DTA} and Chrm4^{CRE}:: Aldh1l1^{WT} mice presented any deficits in balance
467 and coordination.

468 **Telemetry**

469 A TA-F10 temperature and activity probe (Data Sciences International) was implanted
470 in the abdominal cavity of 9-13 weeks old male and female Chrm4^{CRE}:: Aldh1l1^{DTA} and
471 wild type littermate mice (n=8, 19-30 g), using aseptic techniques under a surgical level
472 of isoflurane anaesthesia. Carprofen (10 mg/kg) and buprenorphine (0.1 mg/kg) were
473 s.c. administered 30 min before surgery for pain relief. After surgery, mice were housed
474 individually, and post-operative analgesia was given 6 h (buprenorphine) and 24 h later
475 (carprofen and buprenorphine). One week after surgery, when the animals completely
476 recovered, the cages were placed over the receiver panels and the TA-F10 transmitters
477 were activated. Activity and body temperature data were sampled every 1 min for 10 s
478 and continuously acquired during 4 consecutive days using the Ponemah software
479 (Data Sciences International). The measurements from the final 3 days were averaged
480 together for each mouse. No differences were observed between males and females.

481 **Amphetamine-induced hyperlocomotion**

482 Male and female Chrm4^{CRE}:: Aldh1l1^{DTA} and wild type littermate mice (n=6-7, 10-11
483 weeks old) were placed in an open field arena and the animals were tracked with the
484 ANY-maze software (Stoelting). Habituation lasted for 20 min before being i.p. injected
485 with vehicle (10% Tween 80 in sterile water) or VU0467154 (10 mg/kg). A dose of D-
486 amphetamine (2 mg/kg in saline, i.p.) was administered 20 min later, and locomotor
487 activity was recorded for an additional 90 min. The mobility and distance travelled over
488 time were expressed and averaged per 5 min bins. Total activity data were calculated
489 as the total distance travelled 60 min after the time of D-amphetamine administration.

490 **Burrowing**

491 The voluntary behaviour of removal material from an enclosed tube was assessed in
492 control and prion-infected Chrm4^{CRE}:: Aldh1l1^{DTA} and wild type littermate female mice
493 every week from 9 w.p.i. until survival time. Mice were placed into individual cages (22
494 × 36 cm) with an acrylic clear tube filled with food pellets for 2 h. The burrowing
495 activity was calculated by subtracting the weight of the remaining pellets at the end of
496 the experiment from the starting weight (140 g). Mice were acclimatised to the
497 burrowing cage the week before the start of the test.

498 **Prion mouse model**

499 Male and female Chrm4^{CRE}::MetRS*, Chrm4^{CRE}:: Aldh1l1^{DTA} and Chrm4^{CRE}:: Aldh1l1^{WT}
500 mice aged 3-4 weeks old were i.c. inoculated, under a surgical level of isoflurane
501 anaesthesia, into the right brain parietal lobe with 30 µl of either 1% NBH (Normal
502 Brain Homogenate) or 1% RML prion (Rocky Mountain Laboratories), as previously
503 described (67, 68).

504 **Evaluation of prion disease progression and survival**

505 Chrm4^{CRE}:: Aldh1l1^{DTA} and Chrm4^{CRE}:: Aldh1l1^{WT} control and prion-infected mice were
506 co-housed in mixed-genotype cages to minimise environmental and housing-related
507 bias. Clinical assessment of prion disease progression was performed daily by a trained
508 technician who was blinded to the genotype of the animals, and the scoring protocol
509 followed established criteria consistent with previously published methodologies (7,
510 68, 69). Disease progression was evaluated according to the presence of early indicator
511 and confirmatory signs of prion disease. Early indicator signs included piloerection,
512 mild loss of coordination, erect penis, clasping of hindlimbs when lifted by tail,
513 intermittent generalised tremors, sustained erect ears, rigid tail, discontinued hunched
514 posture, or subdued behaviour. Confirmatory signs of prion disease included righting
515 reflex impairment, sustained hunched posture, dragging of limbs, and/or significant
516 abnormal breathing. Animals were humanely killed when they showed two
517 confirmatory signs or two early indicators plus one confirmatory sign, and the days
518 after inoculation were considered as the survival time.

519 **Preparation of protein extracts and immunoblot analysis**

520 Mice were culled via cervical dislocation, and different regions of the brain were
521 dissected and snap frozen on dry ice. Samples were lysed in RIPA buffer (10 mM Tris-Cl,
522 1 mM EDTA, 1% Triton X-100, 0.1% sodium deoxycholate, 0.1% SDS, 140 mM NaCl, pH
523 7.5) supplemented with protease inhibitor tablets (Cat. #11697498001, Roche) and
524 incubated for 30 min at 4 °C. Lysates were then briefly sonicated (Cat. #12337338,
525 Fisherbrand) with 2 pulses of 15 s at an amplitude of 40% (~50 W) until fully dissolved.
526 Samples were then centrifuged at 10,000 × g for 10 min, supernatants collected, and

527 protein concentration calculated using a BCA assay kit (Cat. #23225, Pierce). Equal
528 concentrations of protein samples were resuspended in Laemmli loading buffer (10%
529 SDS, 300 mM Tris-HCl pH 7.2, 0.05% bromophenol blue, 10% β-mercaptoethanol) and
530 heated at 60°C for 10 min. For the assessment of PrP^{Sc} levels, 60 µg of each lysate were
531 treated with proteinase K (10 µg/ml, Cat. P2308, Sigma-Aldrich) for 10 min at 37°C. The
532 reaction was stopped by the addition of Laemmli sample buffer and boiling at 95°C for
533 5 min. 20-40 µg of each cell lysate were resolved on NuPAGE precast 4-12% gels (Cat.
534 #NP0321, Invitrogen) followed by transfer onto nitrocellulose membranes (Cat.
535 #88018, Thermo Scientific). Protein transfer was verified with Ponceau-S staining (0.2%
536 Ponceau-S red, 1% acetic acid), before membranes were blocked with 5% non-fat dry
537 milk in TBST (25 mM Tris-HCl; pH 7.6, 100 mM NaCl, 0.5% Tween 20) for 1 h at room
538 temperature. Membranes were incubated with the corresponding primary antibodies
539 in the blocking solution overnight at 4°C. After washing three times for 5 min each with
540 TBST, secondary antibodies were added to the membranes for 1 h at RT. Antibodies
541 used in this study are detailed in Tables 1 and 2. Immunoreactive bands were visualised
542 using the Licor Odyssey system and densitometry of fluorescence was measured using
543 Image Studio Lite (Licor Biosciences).

544 **Astrocyte cultures**

545 Murine astrocyte cultures were performed according to the AWESAM protocol (70)
546 with some modifications. Brains from $Chrm4^{CRE}$::MetRS* or WT pups (P0-P5) were
547 collected and immediately placed in ice cold HBSS (ThermoFisher Scientific). After
548 removing of meninges, the cerebellum or the cerebrum were dissected and incubated
549 with 0.05% trypsin-EDTA (Cat. #25300054, ThermoFisher Scientific) at 37°C for 10 min

550 followed by gentle mechanical dissociation. Cells were centrifuged at 1,000 x g for 3
551 min, resuspended in high glucose, Glutamax-supplemented DMEM (Cat. #61965026,
552 Gibco) with 10% Foetal Bovine Serum (Cat. #10500064, Gibco), 100 units/ml penicillin
553 and 100 µg/ml streptomycin (Cat. # 15070063, Gibco), and plated on flasks precoated
554 with poly-D-lysine (100 µg/ml, Cat. #P0899, Sigma-Aldrich). After 7 days in vitro (DIV),
555 the flasks were shaken at 180 rpm for 30 min at 37°C, media changed and further
556 shaken at 240 rpm for 6 h. Astrocytes were detached and seeded at a density of 0.2 x
557 10^6 cells/ml on the corresponding experimental poly-D-lysine plates. After a couple of
558 days, media was replaced with NB+H media, containing Neurobasal (Cat. # 21103049,
559 Gibco) supplemented with B-27 (Cat. #17504044, Gibco), 2 mM Glutamax (Cat. #
560 35050061, Gibco), 10 ng/mL heparin-binding EGF-like growth factor (Cat. #E4643,
561 Sigma-Aldrich), 100 units/ml penicillin and 100 µg/ml streptomycin for 5 days before
562 the start of the experiments.

563 **$ERK_{1/2}$ phosphorylation assay**

564 Cultured primary astrocytes from WT mice were seeded onto 96 well plates precoated
565 with poly-D-lysine at a density of 20,000 cells/well in NB+H media. One week later, the
566 media was replaced, and cells were incubated with 80 µl of Neurobasal without
567 additives for 4 h. Cells were treated for 10 min with vehicle or 10 µM of the M_4 mAChR
568 antagonist VU6028418 before stimulation with the indicated concentrations of
569 oxotremorine for 5 min at 37°C in a final volume of 100 µl. Maximum $ERK_{1/2}$
570 phosphorylation response was obtained by treating the cells with FBS. ERK
571 phosphorylation was evaluated using a Homogenous Time-Resolved FRET (HTRF)-
572 based phospho-ERK (Thr202/Tyr204) cellular kit (Cat. #64ERKPEH, Revvity). Briefly, lysis

573 buffer was added immediately after the end of the stimulation and incubated for 30
574 min. After homogenisation, 16 µl of the lysate were transferred to a 384-well white
575 ProxiPlate (PerkinElmer) and combined with 4 µl HTRF premixed antibodies. for 4 h at
576 room temperature. Fluorescence emission at 665 and 620 nm was measured after 4 h
577 with a PHERAstar plate reader (BMG Labtech) and results were normalised to the
578 response stimulated by FBS.

579 **Immunocytochemistry analysis**

580 Cerebral or cerebellar primary astrocytes from Chrm4^{CRE}::MetRS* mice were grown
581 onto 24 well plates with 13 mm glass coverslips previously treated with poly-D-lysine as
582 indicated above. Cells were fixed with 4% formaldehyde for 1 h at room temperature.
583 Coverslips were then washed 3 times with PBS and blocked with PBS supplemented
584 with 1% BSA and 0.2% Triton X-100 for 1 h. Subsequently, astrocytes were incubated
585 with the indicated primary antibodies diluted in blocking solution overnight at 4°C in a
586 humidity chamber. Detection was achieved using appropriate secondary antibodies
587 conjugated to Alexa Fluor 488 or Alexa Fluor 594 (1:500, Life Technologies) and
588 coverslips were mounted on glass slides using Fluoromount-G with DAPI (ThermoFisher
589 Scientific). Confocal images were acquired with a Zeiss Pascal laser-scanning confocal
590 microscope (LSM) 880 using the LSM image acquisition software.

591 For analysis of c-fos expression, the NB+H media was replaced with non-supplemented
592 Neurobasal, and cells were incubated at 37°C and 5% CO_2 for 4 h, before being
593 stimulated with vehicle or 10 µM oxotremorine for 60 min. To evaluate M_4 mAChR
594 action, cultures were simultaneously treated with vehicle, 10 µM VU0467154 or 5 µM
595 VU6028418. Immunocytochemistry was performed as described above and, for each

596 replicate (n = 3), 8 confocal images (425 µm x 425 µm) per condition were capture,
597 randomly selected using DAPI staining from areas with equivalent number of cells. The
598 images were analysed using ImageJ Fiji (NIH Image). Automatic quantification of c-fos$^+$
599 cells was performed using the "Analyze particle" plugin. M_4 mAChR-expressing
600 astrocytes were manually counted and M_4^+/c-fos$^+$ double stained cells were noted.
601 Total number of cells were also counted automatically with the software tools. The
602 experimental conditions were blinded to the investigator performing the image
603 analysis. This methodology was also used to calculate the proportion of M_4^+ astrocytes
604 present in cerebral and cerebellar cultures.

605 For FUNCAT analysis, Chrm4^{CRE}::MetRS* astrocytes were incubated with 4 mM L-
606 Azidonorleucine hydrochloride (ANL, Tocris) for 24 h. Cells were fixed and blocked as
607 previously described, followed by click chemistry to visualize the ANL-labelled newly
608 synthesized proteins. The Cu(I)-catalysed azide/alkyne cycloaddition (CuAAC) reaction
609 comprised the addition of 0.45 mM $CuSO_4$, 0.9 mM Tris((1-hydroxy-propyl-1H-1,2,3-
610 triazol-4-yl) methyl) amine (THPTA, Cat. #CLK-1010, Jena Bioscience), 0.2 mM Cy3-
611 alkyne (Cat. #777331, Sigma-Aldrich) and 5 mM Sodium ascorbate to the cells for 24 h.
612 Coverslips were washed with PBS containing 0.5 mM EDTA for 10 min, followed by 3
613 washes with blocking solution and the remaining steps of the immunocytochemistry
614 proceeded as indicated above.

615 **Immunohistochemistry**

616 Mice were deeply anaesthetised with isofluorane and then they were transcardially
617 perfused with 20 ml saline solution followed by 20 ml 4% formaldehyde in PBS. Brains
618 were removed and incubated overnight in the same fixative. The whole brain was

619 coronally or sagittally sectioned (50 µm) using a VT1200S vibratome (Leica). After
620 blocking the free-floating sections with PBS supplemented with 0.5% Triton X-100 and
621 1% bovine serum albumin for 1 h at room temperature, they were then incubated with
622 the indicated primary antibodies diluted in blocking solution 24 to 48 h at 4°C.
623 Antibodies used in this study are listed in Tables 1 and 2. Brain sections were washed 3
624 times with PBS, followed by incubation with the corresponding secondary antibodies
625 diluted in blocking solution for 4 h at room temperature. Sections were placed onto 2%
626 gelatine-coated slides and mounted with Fluoromount-G with DAPI. Images were taken
627 with a Zeiss LSM880 confocal microscope using the LSM image acquisition software
628 Zen lite.

629 **Cell counting**

630 The right brain hemisphere of each mouse was sliced in 50 µm coronal sections that
631 were sequentially collected in series containing one every 8th slice. Randomly chosen
632 series of sections were used for immunohistochemistry against GFP and GFAP as
633 described above. Due to the low numbers of M_4^+ astrocytes in the brain, we counted all
634 visible cells positive for both GFP and GFAP within the indicated brain regions in every
635 section of the series under a Zeiss microscope. DAPI images of each section were taken
636 and the area of each region of interest was traced using the freehand drawing tool of
637 ImageJ Fiji. The determined area was then multiplied by the thickness of the section to
638 calculate the reference volume. The density of M_4^+ astrocytes (number of cells/mm^3)
639 was estimated by dividing the total number of positive cells by the reference volume of
640 the corresponding region.

641 The quantification of M_4^+ astrocytes in the arbor vitae of the cerebellum was estimated
642 by unbiased stereology using the physical dissector method adapted to confocal
643 microscopy, as previously described (71). One in eight coronal sections of the
644 cerebellum (50 µm) were immunostained for GFP and GFAP as before. 9-12 confocal
645 counting stacks, acquired with a LSM880 Zeiss microscope, were randomly selected
646 from the whole arbor vitae of the cerebellum. The counting frame size was 150 × 150
647 µm with a thickness of 10.5 µm and a Z-interval of 1.5 µm. The mean cell density of
648 M_4^+ astrocytes was estimated with the counts of the double-labelled cells and the size
649 of the dissector.

650 **Saturation [^{3}H]-NMS binding assay**

651 Striata from homozygous M_4 KO, R26-MetRS* (WT) or heterozygous Chrm4^{CRE}::MetRS*
652 were collected and homogenised in ice-cold HEPES buffer (10 mM HEPES, 1 mM EGTA,
653 1 mM dithiothreitol) containing 10% sucrose and protease inhibitors. The lysate was
654 first centrifuged at 1,000 x g for 10 min at 4°C, the pellet resuspended, re-homogenised
655 and further centrifuged at 20,000 x g for 1 h at 4°C. The resulting pellet containing
656 striatal membranes, was diluted and protein concentration calculated by the Bradford
657 method. 22.5 µg of the striatal membrane preparation were incubated in binding
658 buffer (50 mM HEPEs, 110 mM NaCl, 5.4 mM KCl, 1.8 mM $CaCl_2$, 1 mM $MgSO_4$, 25 mM
659 glucose, 58 mM sucrose, pH 7.4) with increasing concentrations (0.3-5 nM) of the
660 muscarinic receptor antagonist [^{3}H]-N-methyl scopolamine ([^{3}H]-NMS, Cat.
661 #NET636001MC, PerkinElmer) for 1 h at 37°C. Nonspecific binding was determined by
662 the addition of atropine (1 µM) during the incubation with [^{3}H]-NMS. Binding reactions
663 were terminated by rapid filtration over UniFilter GF/C plates (PerkinElmer) pre-soaked

664 in binding buffer, followed by three rapid washes with ice-cold 0.9% NaCl using a filter
665 plate system (Brandel). The plates were then air-dried and 50 µL Microscint-20 liquid
666 scintillation fluid (PerkinElmer) was added to each well. Membrane bound radioactivity
667 was then counted in a Topcount liquid scintillation counter (PerkinElmer). The specific
668 bound counts (dpm) were expressed as fmol/mg protein.

669 **Quantitative RT-PCR**

670 Striata or cerebella from homozygous M_4 KO and R26-MetRS* (WT) mice (10-12 weeks
671 old) were collected and total RNA was isolated using a RNeasy Plus Mini Kit (Cat.
672 #74134, Qiagen), following the manufacturer's instructions. 1 µg total RNA was treated
673 with DNase I (Cat. #79254, Qiagen) and used as template for cDNA synthesis with M-
674 MLV reverse transcriptase (Cat. #28025013, Invitrogen), according to the
675 manufacturer's recommendations. Real-time PCR was performed with probes for
676 Chrm4 (forward 5'-GGAGAAGAAGGCCAAGACTCTGG and reverse 5'-
677 GGCAGTCACACATTCACTGCCTG) and GAPDH as control gene (forward 5'-
678 CGGATTTGGCCGTATTGGG and reverse 5'-CTCGCTCCTGGAAGATGG), 2.4 µl of the cDNA
679 sample as a template and Fast SYBR Green Master Mix (Cat. #4385612, Applied
680 Biosystems) on a Quantstudio 5 Real Time PCR system (ThermoFisher Scientific). The
681 cycling conditions were 50°C for 2 min, 95°C for 10 min, followed by 45 cycles of 95°C
682 for 15 s and 60°C for 1 min. Melting curve analyses were performed for all real-time
683 PCR runs to confirm amplification of only one product and to eliminate false positive
684 results. Quantitative analysis was performed on Quantstudio software (ThermoFisher
685 Scientific), which calculated the threshold cycle (Ct) values. Expression of Chrm4 was
686 defined relative to GAPDH using the $2^{-\Delta\Delta Ct}$ method.

687 **BONCAT purification for LC-MS/MS analysis**

688 Cerebellar primary astrocytes from Chrm4^{CRE}::MetRS* mice grown onto 10 cm dishes
689 as before, were incubated with 4 mM ANL in combination with vehicle, oxotremorine
690 (10 µM) or oxotremorine in combination with VU6028418 (5 µM) for 24 h at 37°C. Cells
691 were lysed in PBS with 0.5% SDS, 0.2% Triton X-100 and proteinase inhibitors, briefly
692 sonicated with 2 pulses of 15 s at an amplitude of 40% (~50 W) and centrifuged at
693 10,000 x g for 10 min at 4°C. Supernatants were collected and protein concentration
694 calculated with a BCA assay kit. 500 µg of protein were heated at 65°C for 5 min
695 followed by incubation with 50 mM iodoacetamide for 2 h at room temperature in the
696 dark. Bio-orthogonal non-canonical amino acid tagging (BONCAT) was performed using
697 150 µM Biotin-PEG4-alkyne (Cat. #764213, Sigma-Aldrich), 0.5 mM $CuSO_4$, 1 mM
698 THPTA and 5 mM sodium ascorbate overnight at 4°C. Buffer exchange was done with
699 PD SpinTrap G-25 columns (Cat. #28-9180-04, Cytvia) and biotinylation of ANL-labelled
700 proteins was confirmed by Western Blot. Ultralink avidin beads (Cat. #53146, Pierce)
701 were used to purify clicked proteins. After overnight incubation at 4°C, beads were
702 loaded into micro-spin columns (Cat. #89879, Pierce) and washed three times with PBS
703 and three washes with ultrapure water. Proteins were eluted with 125 µl of 0.1%
704 Trifluoroacetic acid (TFA) followed by 125 µl of 0.1% TFA with 50% acetonitrile (ACN).
705 Eluted proteins were digested with 4 µg Trypsin/Lys-C (Cat. #V5073, Promega) in S-Trap
706 midi spin columns (Profiti) according to the manufacturer's instructions.

707 Dried peptides were resuspended in 5 % acetonitrile with 0.5 % formic acid for
708 nanoflow liquid chromatography–electrospray ionisation-tandem mass spectrometry
709 (nLC-ESI-MS/MS) analysis. The samples were loaded onto a C_{18} Acclaim PepMap

710 trapping column (ThermoFisher Scientific) using an UltiMate3000 RSLCnano System
711 (ThermoFisher Scientific). Peptide separation was performed on a Pepmap C_{18} reversed
712 phase column (2 µm, 75 µm × 50 cm, pore size 100 Å, Cat. #164540, ThermoFisher
713 Scientific) by a gradient formed by mobile phase A (0.1% formic acid) and B (80% ACN,
714 0.08% formic acid), with increasing concentrations of solvent B running from 4% for 10
715 min, 60% for 170 min to 99% for 15 min at a fixed solvent flow rate of 0.3 µl/min.
716 Eluted peptides were electrosprayed into an Orbitrap Elite MS (ThermoFisher Scientific)
717 using a NanoMate Triversa (Advion Biosciences) ion source at 1.7 kV. The mass
718 spectrometer was operated using full-scan MS spectra (m/z 375–1,500) at a resolution
719 of 120,000 RP, followed by top speed (3s) high energy collision dissociation (HCD)
720 fragmentation detection of the top precursor ions. Ion fragmentation was performed
721 by top speed (3s) high energy collision dissociation (HCD) and the top precursor ions
722 were detected at a resolution of 60,000 in MS2 spectra. HCD energy and isolation
723 width was adjusted depending on charge of the precursor ions (a width of 1.2 m/z with
724 40% HCD for 2^+ ions, 0.7 m/z with 38% for 3^+, and 0.5 m/z with 38% HCD for 4^+-6^+). The
725 resulting MS/MS spectra were analysed for protein identification using Proteome
726 Discoverer software 2.4 (ThermoFisher Scientific) and searched against the murine
727 UniProtKB/Swiss-Prot database using Mascot software (Matrix Science) with peptide
728 tolerance set to 10 ppm and fragment ion mass tolerance of 0.3 Da. The
729 carbamidomethylation of cysteine was programmed as fixed modification, while the
730 oxidation of methionine, the deamidation of asparagine and glutamine, the
731 replacement of methionine for ANL-PEG-biotin and the iodination of tyrosine were set
732 as variables. Proteins present in at least 2 independent experiments were considered

733 for GO enrichment analysis to identify overrepresented biological processes using
734 PANTHER (72) with a Fisher's exact test and a cutoff of FDR ≤0.05.

735 **Statistical analysis**

736 All data were expressed as mean ± SEM of at least 3 independent experiments.
737 Statistical significance was determined by two-tailed Student's *t* test, one-way ANOVA
738 with Tukey's post hoc correction or two-way ANOVA followed by a Tukey's or
739 Bonferroni's post hoc test, as indicated. For $ERK_{1/2}$ phosphorylation assays the
740 concentration–response data were plotted on a log axis, fitted to a three-parameter
741 sigmoidal curve and extra sum-of-squares F test applied to determine whether
742 differences in pEC_{50} existed. The Kaplan-Meier plot survival analyses were compared
743 using the Gehan-Breslow-Wilcoxon test. Significance was considered a *p* value smaller
744 than 0.05 (*$p < 0.05$, **$p < 0.01$, ***$p < 0.001$). Statistical analysis and graph plotting
745 was performed using GraphPad Prism software.

746 **Table 1: Primary antibodies.** ICC, immunocytochemistry; IHC, immunohistochemistry;
747 WB, western blot.

Antibody	Supplier	Cat. No	Host	Dilution	Use
S100β	Proteintech	15146-1-AP	Rabbit	1:500	ICC
c-fos	Abcam	ab190289	Rabbit	1:1,000	ICC
GFAP	Abcam	ab7260	Rabbit	1:500	ICC
GFP	Abcam	ab6673	Goat	1:500	ICC
S100β	Proteintech	15146-1-AP	Rabbit	1:1,000	IHC
Calbindin-D28k	Proteintech	14479-1-AP	Rabbit	1:1,000	IHC
GBP2	Proteintech	11854-1-AP	Rabbit	1:500	IHC
GFAP	Abcam	ab7260	Rabbit	1:1,000	IHC
GFAP	Sigma-Aldrich	G3893	Mouse	1:2,000	IHC
GFP	Abcam	ab6673	Goat	1:1,000	IHC
GFP	Abcam	Ab6556	Rabbit	1:1,000	IHC

Iba1	Abcam	ab178846	Rabbit	1:1,000	IHC
MAP2	Biolegend	822501	Chicken	1:1,000	IHC
MT3	Proteintech	12179-1-AP	Rabbit	1:500	IHC
Myelin basic protein (MBP)	Proteintech	10458-1-AP	Rabbit	1:2,000	IHC
NDRG2	Abcam	ab174850	Rabbit	1:1,000	IHC
Apolipoprotein E (APO-E)	Abcam	ab183596	Rabbit	1:1,000	WB
Chrm4	Aviva	OASG0431	Rabbit	1:500	WB
Clusterin	R&D Systems	AF2747	Goat	1:2,000	WB
GFAP	Sigma-Aldrich	G3893	Mouse	1:1,000	WB
GFP	Invitrogen	A-11122	Rabbit	1:1,000	WB
Iba1	Abcam	ab178846	Rabbit	1:2,000	WB
IRDye 800CW Streptavidin	Li-Cor Biosciences	926-32230	-	1:5,000	WB
Myelin basic protein (MBP)	Proteintech	10458-1-AP	Rabbit	1:4,000	WB
Prion protein (Prp)	Abcam	ab61409	Mouse	1:1,000	WB
SerpinA3N	R&D Systems	AF4709	Goat	1:1,000	WB
Vimentin	R&D Systems	MAB21052	Mouse	1:2,000	WB
α-tubulin	Abcam	ab7291	Mouse	1:10,000	WB

748 **Table 2: Secondary antibodies.** ICC, immunocytochemistry; IHC,

749 immunohistochemistry; WB, western blot.

Antibody	Supplier	Cat. No	Host	Dilution	Use
Anti-Rabbit Alexa Fluor Plus 647	Invitrogen	A32795	Donkey	1:500	ICC
Anti-Chicken Alexa Fluor 594	Invitrogen	A11042	Goat	1:1,000	IHC
Anti-Rabbit Alexa Fluor 488	Invitrogen	A32731	Goat	1:1,000	IHC
Anti-Goat Alexa Fluor Plus 488	Invitrogen	A32814	Donkey	1:1,000/ 1:500	IHC/ ICC
Anti-Mouse Alexa Fluor Plus 594	Invitrogen	A32744	Donkey	1:1,000/ 1:500	IHC/ ICC
Anti-Rabbit Alexa Fluor Plus 594	Invitrogen	A32754	Donkey	1:1,000/ 1:500	IHC/ ICC
IRDye 680RD Anti-Goat	Li-Cor Biosciences	925-68074	Donkey	1:5,000	WB

IRDye 680RD Anti-Mouse	Li-Cor Biosciences	925-68072	Donkey	1:5,000	WB/ IHC
IRDye 800CW Anti-Mouse	Li-Cor Biosciences	926-32212	Donkey	1:5,000	WB
IRDye 800CW Anti-Rabbit	Li-Cor Biosciences	925-32213	Donkey	1:5,000	WB

750

751 ## Abbreviations

752 CNS: central nervous system, $ERK_{1/2}$: extracellular signal-regulated kinases 1/2, GFAP:
753 glial fibrillary acidic protein, GFP: green fluorescent protein, eGFP: enhanced green
754 fluorescent protein, GPCR: G protein-coupled receptor, mAChR: muscarinic
755 acetylcholine receptor, NBH: normal brain homogenate, PAM: positive allosteric
756 modulator, pEC_{50}: half maximal response, Prp^{Sc}: scrapie prion protein, RML: rocky
757 mountain laboratory, w.p.i: weeks post-inoculation.

758 # Declarations

759 ## Ethics approval

760 All animal experiments were conducted in accordance with the UK Home Office Animal
761 Procedures Act (1986) and all procedures were approved by the University of Glasgow
762 Animal Welfare and Ethical Review Board.

763 ## Consent for publication

764 Not applicable

765 ## Availability of data and materials

766 Source data are provided with this paper.

767 ## Competing Interests

768 The authors declare no competing interests.

769 ## Funding

770 This work was supported by grants from the Wellcome Trust (Collaborative Award
771 201529/Z/16/Z and Discovery Award 307319/Z/23/Z).

772 ## Author's Contributions

773 GST conducted the experiments, developed the study design and wrote the paper, ABT
774 lead the study design and wrote the paper, GM contributed to the study design and
775 writing of the paper, CM managed the mouse colonies and breeding and helped to
776 conduct the animal experiments, CWL contributed with the muscarinic antagonist
777 VU6028418 and the M_4 mAChR positive allosteric modulator VU0467154 and CKJ
778 contributed with pharmacokinetic, pharmacology and metabolism data of these
779 ligands.

780 ## Acknowledgments

781 The authors would like to thank the staff of the University of Glasgow Biomedical
782 Services, genOway for generation of the muscarinic receptor genetically modified mice.
783 The authors would also like to acknowledge the assistance of Dr. Karen Fairlie-Clarke to
784 this work.

785

786 ## References

787 1. Kaul I, Sawchak S, Correll CU, Kakar R, Breier A, Zhu H, et al. Efficacy and safety of the
788 muscarinic receptor agonist KarXT (xanomeline-trospium) in schizophrenia

789 (EMERGENT-2) in the USA: results from a randomised, double-blind, placebo-
790 controlled, flexible-dose phase 3 trial. Lancet. 2024;403(10422):160-70.
791 2. Kaul I, Sawchak S, Walling DP, Tamminga CA, Breier A, Zhu H, et al. Efficacy and Safety
792 of Xanomeline-Trospium Chloride in Schizophrenia: A Randomized Clinical Trial. JAMA
793 Psychiatry. 2024;81(8):749-56.
794 3. Mei F, Lehmann-Horn K, Shen YA, Rankin KA, Stebbins KJ, Lorrain DS, et al. Accelerated
795 remyelination during inflammatory demyelination prevents axonal loss and improves
796 functional recovery. Elife. 2016;5.
797 4. Wang F, Yang YJ, Yang N, Chen XJ, Huang NX, Zhang J, et al. Enhancing Oligodendrocyte
798 Myelination Rescues Synaptic Loss and Improves Functional Recovery after Chronic
799 Hypoxia. Neuron. 2018;99(4):689-701 e5.
800 5. Wang F, Ren SY, Chen JF, Liu K, Li RX, Li ZF, et al. Myelin degeneration and diminished
801 myelin renewal contribute to age-related deficits in memory. Nat Neurosci.
802 2020;23(4):481-6.
803 6. Chen JF, Liu K, Hu B, Li RR, Xin W, Chen H, et al. Enhancing myelin renewal reverses
804 cognitive dysfunction in a murine model of Alzheimer's disease. Neuron.
805 2021;109(14):2292-307 e5.
806 7. Dwomoh L, Rossi M, Scarpa M, Khajehali E, Molloy C, Herzyk P, et al. M(1) muscarinic
807 receptor activation reduces the molecular pathology and slows the progression of
808 prion-mediated neurodegenerative disease. Sci Signal. 2022;15(760):eabm3720.
809 8. Abd-Elrahman KS, Colson TL, Sarasija S, Ferguson SSG. A M1 muscarinic acetylcholine
810 receptor-specific positive allosteric modulator VU0486846 reduces neurogliosis in
811 female Alzheimer's mice. Biomed Pharmacother. 2024;173:116388.
812 9. Pannell M, Meier MA, Szulzewsky F, Matyash V, Endres M, Kronenberg G, et al. The
813 subpopulation of microglia expressing functional muscarinic acetylcholine receptors
814 expands in stroke and Alzheimer's disease. Brain Struct Funct. 2016;221(2):1157-72.
815 10. Andre C, Dos Santos G, Koulakoff A. Muscarinic receptor profiles of mouse brain
816 astrocytes in culture vary with their tissue of origin but differ from those of neurons.
817 Eur J Neurosci. 1994;6(11):1702-9.
818 11. Endo F, Kasai A, Soto JS, Yu X, Qu Z, Hashimoto H, et al. Molecular basis of astrocyte
819 diversity and morphology across the CNS in health and disease. Science.
820 2022;378(6619):eadc9020.
821 12. Zhang Y, Chen K, Sloan SA, Bennett ML, Scholze AR, O'Keeffe S, et al. An RNA-
822 sequencing transcriptome and splicing database of glia, neurons, and vascular cells of
823 the cerebral cortex. J Neurosci. 2014;34(36):11929-47.
824 13. Yao Z, van Velthoven CTJ, Kunst M, Zhang M, McMillen D, Lee C, et al. A high-resolution
825 transcriptomic and spatial atlas of cell types in the whole mouse brain. Nature.
826 2023;624(7991):317-32.
827 14. Alvarez-Castelao B, Schanzenbacher CT, Hanus C, Glock C, Tom Dieck S, Dorrbaum AR,
828 et al. Cell-type-specific metabolic labeling of nascent proteomes in vivo. Nat
829 Biotechnol. 2017;35(12):1196-201.
830 15. Sjostedt E, Zhong W, Fagerberg L, Karlsson M, Mitsios N, Adori C, et al. An atlas of the
831 protein-coding genes in the human, pig, and mouse brain. Science. 2020;367(6482).
832 16. Buckley NJ, Bonner TI, Brann MR. Localization of a family of muscarinic receptor
833 mRNAs in rat brain. J Neurosci. 1988;8(12):4646-52.
834 17. Heintz N. Gene expression nervous system atlas (GENSAT). Nat Neurosci.
835 2004;7(5):483.
836 18. Vilaro MT, Wiederhold KH, Palacios JM, Mengod G. Muscarinic cholinergic receptors in
837 the rat caudate-putamen and olfactory tubercle belong predominantly to the m4 class:
838 in situ hybridization and receptor autoradiography evidence. Neuroscience.
839 1991;40(1):159-67.

19. Arenander AT, de Vellis J, Herschman HR. Induction of c-fos and TIS genes in cultured rat astrocytes by neurotransmitters. J Neurosci Res. 1989;24(1):107-14.
20. Bubser M, Bridges TM, Dencker D, Gould RW, Grannan M, Noetzel MJ, et al. Selective activation of M4 muscarinic acetylcholine receptors reverses MK-801-induced behavioral impairments and enhances associative learning in rodents. ACS Chem Neurosci. 2014;5(10):920-42.
21. Spock M, Carter TR, Bollinger KA, Han C, Baker LA, Rodriguez AL, et al. Discovery of VU6028418: A Highly Selective and Orally Bioavailable M(4) Muscarinic Acetylcholine Receptor Antagonist. ACS Med Chem Lett. 2021;12(8):1342-9.
22. Tsai HH, Li H, Fuentealba LC, Molofsky AV, Taveira-Marques R, Zhuang H, et al. Regional astrocyte allocation regulates CNS synaptogenesis and repair. Science. 2012;337(6092):358-62.
23. Cerrato V. Cerebellar Astrocytes: Much More Than Passive Bystanders In Ataxia Pathophysiology. J Clin Med. 2020;9(3).
24. Gould RW, Grannan MD, Gunter BW, Ball J, Bubser M, Bridges TM, et al. Cognitive enhancement and antipsychotic-like activity following repeated dosing with the selective M(4) PAM VU0467154. Neuropharmacology. 2018;128:492-502.
25. Foster DJ, Wilson JM, Remke DH, Mahmood MS, Uddin MJ, Wess J, et al. Antipsychotic-like Effects of M4 Positive Allosteric Modulators Are Mediated by CB2 Receptor-Dependent Inhibition of Dopamine Release. Neuron. 2016;91(6):1244-52.
26. Pancani T, Bolarinwa C, Smith Y, Lindsley CW, Conn PJ, Xiang Z. M4 mAChR-mediated modulation of glutamatergic transmission at corticostriatal synapses. ACS Chem Neurosci. 2014;5(4):318-24.
27. Moehle MS, Pancani T, Byun N, Yohn SE, Wilson GH, 3rd, Dickerson JW, et al. Cholinergic Projections to the Substantia Nigra Pars Reticulata Inhibit Dopamine Modulation of Basal Ganglia through the M(4) Muscarinic Receptor. Neuron. 2017;96(6):1358-72 e4.
28. Jeon J, Dencker D, Wortwein G, Woldbye DP, Cui Y, Davis AA, et al. A subpopulation of neuronal M4 muscarinic acetylcholine receptors plays a critical role in modulating dopamine-dependent behaviors. J Neurosci. 2010;30(6):2396-405.
29. Zimmer TS, Orr AL, Orr AG. Astrocytes in selective vulnerability to neurodegenerative disease. Trends Neurosci. 2024;47(4):289-302.
30. Endo F. Deciphering the spectrum of astrocyte diversity: Insights into molecular, morphological, and functional dimensions in health and neurodegenerative diseases. Neurosci Res. 2024.
31. Moulson AJ, Squair JW, Franklin RJM, Tetzlaff W, Assinck P. Diversity of Reactive Astrogliosis in CNS Pathology: Heterogeneity or Plasticity? Front Cell Neurosci. 2021;15:703810.
32. Tahir W, Thapa S, Schatzl HM. Astrocyte in prion disease: a double-edged sword. Neural Regen Res. 2022;17(8):1659-65.
33. Hartmann K, Sepulveda-Falla D, Rose IVL, Madore C, Muth C, Matschke J, et al. Complement 3(+)-astrocytes are highly abundant in prion diseases, but their abolishment led to an accelerated disease course and early dysregulation of microglia. Acta Neuropathol Commun. 2019;7(1):83.
34. Akhtar S, Wenborn A, Brandner S, Collinge J, Lloyd SE. Sex effects in mouse prion disease incubation time. PLoS One. 2011;6(12):e28741.
35. Liu Y, Guo J, Matoga M, Korotkova M, Jakobsson PJ, Aguzzi A. NG2 glia protect against prion neurotoxicity by inhibiting microglia-to-neuron prostaglandin E2 signaling. Nat Neurosci. 2024;27(8):1534-44.
36. Denouel A, Brandel JP, Seilhean D, Laplanche JL, Elbaz A, Haik S. The role of environmental factors on sporadic Creutzfeldt-Jakob disease mortality: evidence from an age-period-cohort analysis. Eur J Epidemiol. 2023;38(7):757-64.

892 37. Myslivecek J, Farar V, Valuskova P. M(4) muscarinic receptors and locomotor activity
893 regulation. Physiol Res. 2017;66(Suppl 4):S443-S55.
894 38. Chambers NE, Millett M, Moehle MS. The muscarinic M4 acetylcholine receptor
895 exacerbates symptoms of movement disorders. Biochem Soc Trans. 2023;51(2):691-
896 702.
897 39. Nunes EJ, Addy NA, Conn PJ, Foster DJ. Targeting the Actions of Muscarinic Receptors
898 on Dopamine Systems: New Strategies for Treating Neuropsychiatric Disorders. Annu
899 Rev Pharmacol Toxicol. 2024;64:277-89.
900 40. Camandola S. Astrocytes, emerging stars of energy homeostasis. Cell Stress.
901 2018;2(10):246-52.
902 41. Gonzalez-Garcia I, Garcia-Caceres C. Hypothalamic Astrocytes as a Specialized and
903 Responsive Cell Population in Obesity. Int J Mol Sci. 2021;22(12).
904 42. Yang L, Qi Y, Yang Y. Astrocytes control food intake by inhibiting AGRP neuron activity
905 via adenosine A1 receptors. Cell Rep. 2015;11(5):798-807.
906 43. Chen N, Sugihara H, Kim J, Fu Z, Barak B, Sur M, et al. Direct modulation of GFAP-
907 expressing glia in the arcuate nucleus bi-directionally regulates feeding. Elife. 2016;5.
908 44. Herrera Moro Chao D, Kirchner MK, Pham C, Foppen E, Denis RGP, Castel J, et al.
909 Hypothalamic astrocytes control systemic glucose metabolism and energy balance. Cell
910 Metab. 2022;34(10):1532-47 e6.
911 45. MacDonald AJ, Holmes FE, Beall C, Pickering AE, Ellacott KLJ. Regulation of food intake
912 by astrocytes in the brainstem dorsal vagal complex. Glia. 2020;68(6):1241-54.
913 46. Clyburn C, Carson KE, Smith CR, Travagli RA, Browning KN. Brainstem astrocytes control
914 homeostatic regulation of caloric intake. J Physiol. 2023;601(4):801-29.
915 47. Cai P, Huang SN, Lin ZH, Wang Z, Liu RF, Xiao WH, et al. Regulation of wakefulness by
916 astrocytes in the lateral hypothalamus. Neuropharmacology. 2022;221:109275.
917 48. Brancaccio M, Edwards MD, Patton AP, Smyllie NJ, Chesham JE, Maywood ES, et al. Cell-
918 autonomous clock of astrocytes drives circadian behavior in mammals. Science.
919 2019;363(6423):187-92.
920 49. Nimmerjahn A, Mukamel EA, Schnitzer MJ. Motor behavior activates Bergmann glial
921 networks. Neuron. 2009;62(3):400-12.
922 50. Paukert M, Agarwal A, Cha J, Doze VA, Kang JU, Bergles DE. Norepinephrine controls
923 astroglial responsiveness to local circuit activity. Neuron. 2014;82(6):1263-70.
924 51. Corkrum M, Covelo A, Lines J, Bellocchio L, Pisansky M, Loke K, et al. Dopamine-Evoked
925 Synaptic Regulation in the Nucleus Accumbens Requires Astrocyte Activity. Neuron.
926 2020;105(6):1036-47 e5.
927 52. Schweinhuber SK, Messerschmidt T, Hansch R, Korte M, Rothkegel M. Profilin isoforms
928 modulate astrocytic morphology and the motility of astrocytic processes. PLoS One.
929 2015;10(1):e0117244.
930 53. Lee SJ, Seo BR, Koh JY. Metallothionein-3 modulates the amyloid beta endocytosis of
931 astrocytes through its effects on actin polymerization. Mol Brain. 2015;8(1):84.
932 54. Zhou J, Zhang L, Peng J, Zhang X, Zhang F, Wu Y, et al. Astrocytic LRP1 enables
933 mitochondria transfer to neurons and mitigates brain ischemic stroke by suppressing
934 ARF1 lactylation. Cell Metab. 2024;36(9):2054-68 e14.
935 55. Romeo R, Glotzbach K, Scheller A, Faissner A. Deletion of LRP1 From Astrocytes
936 Modifies Neuronal Network Activity in an in vitro Model of the Tripartite Synapse.
937 Front Cell Neurosci. 2020;14:567253.
938 56. Gogliotti RG, Fisher NM, Stansley BJ, Jones CK, Lindsley CW, Conn PJ, et al. Total RNA
939 Sequencing of Rett Syndrome Autopsy Samples Identifies the M(4) Muscarinic
940 Receptor as a Novel Therapeutic Target. J Pharmacol Exp Ther. 2018;365(2):291-300.
941 57. Achilly NP, He LJ, Kim OA, Ohmae S, Wojaczynski GJ, Lin T, et al. Deleting Mecp2 from
942 the cerebellum rather than its neuronal subtypes causes a delay in motor learning in
943 mice. Elife. 2021;10.

944 58. Patani R, Hardingham GE, Liddelow SA. Functional roles of reactive astrocytes in
945 neuroinflammation and neurodegeneration. Nat Rev Neurol. 2023;19(7):395-409.
946 59. Makarava N, Chang JC, Kushwaha R, Baskakov IV. Region-Specific Response of
947 Astrocytes to Prion Infection. Front Neurosci. 2019;13:1048.
948 60. Makarava N, Chang JC, Molesworth K, Baskakov IV. Region-specific glial homeostatic
949 signature in prion diseases is replaced by a uniform neuroinflammation signature,
950 common for brain regions and prion strains with different cell tropism. Neurobiol Dis.
951 2020;137:104783.
952 61. Carroll JA, Striebel JF, Rangel A, Woods T, Phillips K, Peterson KE, et al. Prion Strain
953 Differences in Accumulation of PrPSc on Neurons and Glia Are Associated with Similar
954 Expression Profiles of Neuroinflammatory Genes: Comparison of Three Prion Strains.
955 PLoS Pathog. 2016;12(4):e1005551.
956 62. Munoz-Castro C, Serrano-Pozo A. Astrocyte-Neuron Interactions in Alzheimer's Disease.
957 Adv Neurobiol. 2024;39:345-82.
958 63. Carter SF, Herholz K, Rosa-Neto P, Pellerin L, Nordberg A, Zimmer ER. Astrocyte
959 Biomarkers in Alzheimer's Disease. Trends Mol Med. 2019;25(2):77-95.
960 64. Makarava N, Mychko O, Chang JC, Molesworth K, Baskakov IV. The degree of astrocyte
961 activation is predictive of the incubation time to prion disease. Acta Neuropathol
962 Commun. 2021;9(1):87.
963 65. Gomeza J, Zhang L, Kostenis E, Felder CC, Bymaster FP, Brodkin J, et al. Generation and
964 pharmacological analysis of M2 and M4 muscarinic receptor knockout mice. Life Sci.
965 2001;68(22-23):2457-66.
966 66. Guyenet SJ, Furrer SA, Damian VM, Baughan TD, La Spada AR, Garden GA. A simple
967 composite phenotype scoring system for evaluating mouse models of cerebellar ataxia.
968 J Vis Exp. 2010(39).
969 67. Mallucci G, Dickinson A, Linehan J, Klohn PC, Brandner S, Collinge J. Depleting neuronal
970 PrP in prion infection prevents disease and reverses spongiosis. Science.
971 2003;302(5646):871-4.
972 68. Scarpa M, Molloy C, Jenkins L, Strellis B, Budgett RF, Hesse S, et al. Biased M1
973 muscarinic receptor mutant mice show accelerated progression of prion
974 neurodegenerative disease. Proc Natl Acad Sci U S A. 2021;118(50).
975 69. Mirabile I, Jat PS, Brandner S, Collinge J. Identification of clinical target areas in the
976 brainstem of prion-infected mice. Neuropathol Appl Neurobiol. 2015;41(5):613-30.
977 70. Wolfes AC, Dean C. Culturing In Vivo-like Murine Astrocytes Using the Fast, Simple, and
978 Inexpensive AWESAM Protocol. J Vis Exp. 2018(131).
979 71. Llorens-Martin M, Torres-Aleman I, Trejo JL. Pronounced individual variation in the
980 response to the stimulatory action of exercise on immature hippocampal neurons.
981 Hippocampus. 2006;16(5):480-90.
982 72. Thomas PD, Ebert D, Muruganujan A, Mushayahama T, Albou LP, Mi H. PANTHER:
983 Making genome-scale phylogenetics accessible to all. Protein Sci. 2022;31(1):8-22.

984 ## Figure legends

985 **Fig. 1: M_4 mAChR is expressed in neuronal and disperse astrocytic populations**
986 **throughout the brain. a**, Schematic overview of the breeding between mice driving
987 CRE recombinase from the *Chrm4* promoter (Chrm4^{CRE}) with mice carrying the
988 inducible transgene for expression of GFP and MetRS* L274G (R26-MetRS*). The

989 distribution of M_4 mAChR expressing cells can be detected in the resulting
990 Chrm4^{CRE}::MetRS* mice by GFP immunostaining (green) in a brain sagittal section. **b**,
991 Representative confocal images showing co-immunostaining of GFP (green) with the
992 neuronal marker MAP2 (magenta) in areas of the cortex, striatum and hippocampus.
993 The white square insets indicate the enlarged areas showed in the panels below by
994 each individual channel. **c**, Representative confocal images showing co-localisation of
995 GFP expressing cells with the astrocyte marker GFAP (magenta) in the hypothalamus
996 and the brainstem. Scale bar for panel **a** is 250 µm, and for **b** and **c**, 25 µm.

997 **Fig. 2: The cerebellum contains a diverse array of cells expressing M_4 mAChR. a**,
998 Distribution of M_4 mAChR expressing cells labelled with GFP staining in a sagittal
999 section of the cerebellum of Chrm4^{CRE}::MetRS* mice. **b**, Co-immunostaining of GFP-
1000 labelled M_4^+ cells with Calbindin in the Purkinje layer of the cerebellum of
1001 Chrm4^{CRE}::MetRS* mice. **c**, Immunohistochemistry analysis of different populations of
1002 GFAP positive astrocytes (magenta) co-expressing M_4 mAChR (green) in the cerebellar
1003 cortex (left panel), cerebellar nuclei (CN, middle panel) and white matter region (right
1004 panel). Arrowheads indicate M_4^+ astrocytes. Scale bar for panels **a** and **b** is 250 µm, and
1005 for **c**, 25 µm.

1006 **Fig. 3: Role of M_4 mAChR in cerebellar astrocytic cultures of Chrm4^{CRE}::MetRS*. a**,
1007 Immunostaining of cerebral or cerebellar astrocyte cultures from Chrm4^{CRE}::MetRS*
1008 animals detecting M_4 expressing cells with GFP (green) and the astrocyte marker GFAP
1009 (magenta). **b**, Quantification of the proportion of M_4^+ astrocytes in cerebral and
1010 cerebellar cultures relative to the total astrocytes present in the preparation (n = 5 - 9).
1011 **c**, The percentage of the population of M_4^+ astrocytes co-expressing c-fos was

1012 estimated in astrocyte cerebellar cultures after stimulation with Oxotremorine (Oxo, 10
1013 µM), a combination of Oxo and the M_4 mAChR PAM VU0467154 (VU154, 10 µM) or
1014 Oxo plus the M_4 mAChR antagonist VU6028418 (VU418, 5 µM) for 60 min (n= 5). **d**,
1015 Representative confocal images showing M_4 expressing astrocytes (green) co-stained
1016 with c-fos (magenta) in cerebellar cultures after treatment with Vehicle (Control), Oxo
1017 or a combination of Oxo and VU154 or Oxo with VU418, as indicated in **c**. **e**, Venn
1018 diagram showing the newly synthesised proteins (NSPs) exclusively identified from M_4^+
1019 cerebellar astrocytes after treatment with ANL (4 mM) in combination with Vehicle,
1020 Oxo (10 µM) or Oxo and VU418 (5 µM). **f**, Analysis of enriched GO annotations (Fisher's
1021 exact test performed with Panther v. 17.0) in M_4^+ cerebellar astrocytes after treatment
1022 with ANL in basal conditions (n = 2). The size of each circle represents the number of
1023 genes, and the colour intensity indicates the $-\log_{10}$ *p* value adjusted by Benjamini-
1024 Hochberg method assigned to the corresponding GO term. **g**, Gene ontology biological
1025 processes which are significantly enriched from the nascent proteins synthesized after
1026 activation of M_4 mAChR in M_4^+ cerebellar astrocytes (NSPs exclusively found after Oxo
1027 treatment and not identified when the M_4 antagonist is present). Graphs depict means
1028 ± SEM and statistical significance was calculated by two-tailed unpaired *t* test (**b**), or
1029 one-way ANOVA followed by Tukey's pot hoc test (**c**) (*$p < 0.05$, **$p < 0.01$, ***$p <$
1030 0.01,). Scale bars, 25 µm.

1031 **Fig. 4: Selective ablation of M_4^+ astrocytes leads to deficits in locomotor activity. a**,
1032 Depiction showing the breeding overview between the $Chrm4^{CRE}$ animals with the
1033 hemizygous Aldh1l1-eGFP,-DTA mice, that express eGFP under the astrocyte promoter
1034 *Aldh1l1* and an inducible diphteria toxin A when Cre recombinase is present. This
1035 mating results in $Chrm4^{CRE}$:: $Aldh1l1^{DTA}$ mice (DTA^{M4}*) with ablated astrocytes that

1036 express the M_4 mAChR, and the control littermates Chrm4^{CRE}:: Aldh1l1^{WT} (WT^{M4}*), wild
1037 type for the floxed gene. **b**, Average animal weight per group over time (n = 6-10). **c**,
1038 Comparison of the performance on the accelerated rotarod test between DTA^{M4}* and
1039 WT^{M4}* mice during 4 consecutive weeks (n = 10). **d**, Activity of mice in and open field
1040 test measuring the time spent in the central area of the apparatus (n = 15-18). **e**, Total
1041 distance travelled over the whole area of the open field arena. **f**, Analysis of the
1042 anxiety-like behaviour of DTA^{M4}* and WT^{M4}* mice measuring the time spent in the
1043 open arms of an elevated plus maze (n = 15-18). **g**, Locomotor activity in DTA^{M4}*
1044 animals compared to WT^{M4}* littermates measured by telemetry. The graph depicts the
1045 profile of activity counts averaged over 3 days of recording and plotted every five min.
1046 Mice experience a 12/12 h light/dark cycle, with the dark cycle shown in the shaded
1047 area (n = 8). **h**, Comparison of the average telemetry activity counts during the 12-h
1048 light and dark phases between DTA^{M4}* and WT^{M4}* mice. **i**, Effect of VU0467154
1049 (VU154, 10 mg/kg) or vehicle (Veh) to counteract the amphetamine-induced
1050 hyperlocomotion (2 mg/kg) in DTA^{M4}* and WT^{M4}* mice. **j**, Total distance travelled
1051 during the 60 min period following D-amphetamine administration. (n = 6-7). Data are
1052 means ± SEM and statistical significance was calculated by two-tailed unpaired *t* test or
1053 one-way ANOVA followed by Bonferroni's pot hoc test when analysis involved more
1054 than two groups (*$p < 0.05$, **$p < 0.01$).

1055 **Fig 5. Regional and temporal expansion in the number of the M_4^+ astrocytes during**
1056 **mouse prion disease. a**, Representative confocal images of GFP-labelled M_4^+ cells in
1057 coronal brain sections from Chrm4^{CRE}::MetRS* animals after 20 w.p.i. of RML prion
1058 inoculation (right) or control animals treated with NBH (left). Panels below show a
1059 detail of M_4^+ astrocytes (arrowheads) co-stained with GFP (green) and GFAP (magenta)

1060 from the thalamic areas indicated with white square insets. **b**, Confocal images
1061 showing M_4^+ astrocytes co-stained with GFP (green) and GFAP (magenta) in the
1062 cerebellar nuclei of Chrm4^{CRE}::MetRS* mice after 20 w.p.i. of RML prion disease (right)
1063 or NBH controls (left). **c**, Regional and temporal spreading pattern of the density of M_4^+
1064 astrocytes at different stages of RML prion disease in Chrm4^{CRE}::MetRS* mice plotted
1065 on brain anatomical maps. Darker red sections represent regions with higher densities
1066 in M_4^+ astrocytes, while not quantified areas are depicted in grey. **d**, Quantification of
1067 M_4^+ astrocytes density across brain regions in Chrm4^{CRE}::MetRS* mice treated with
1068 RML prion after 15, 17 and 23 w.p.i. and compared to control animals inoculated with
1069 NBH (n = 2-3). **e**, Representative confocal images showing co-localisation of GFP
1070 (green), GFAP (magenta) and GBP2 in the hippocampus and thalamus of 20 w.p.i. RML-
1071 inoculated Chrm4^{CRE}::MetRS* mice. Scale bar in **a** is 250 µm, and 25 µm in **b** and **e**.
1072 Data shown are represented as mean ± SEM. Statistical significance was calculated by
1073 two-way ANOVA followed by Bonferroni's post hoc test (***$p < 0.001$, **$p < 0.01$).

1074 **Fig. 6. Ablation of M_4^+ astrocytes prolongs survival and reduces Prp^{Sc} deposition in**
1075 **the cerebellum of prion-infected mice. a**, Evaluation of progressive motor deficits by
1076 rotarod in prion-diseased DTA^{M4}* and WT^{M4}* mice from 12 w.p.i (n = 8-12). **b**,
1077 Burrowing behaviour (percentage of food pellets displaced from the tube) of control or
1078 prion-infected DTA^{M4}* and WT^{M4}* mice assessed from 12 w.p.i. (n = 5 for NBH, n = 10-
1079 12 for RML). **c**, Kaplan-Meier plot showing a significant increase in survival probability
1080 for RML-prion inoculated mice after ablation of M_4^+ astrocytes (DTA^{M4}*) compared to
1081 wild-type littermates (WT^{M4}*) (n = 22 - 25). Sex-differences are observed when survival
1082 curves are compared between females (**d**, n = 10-17) and males (**e**, n = 8-12). Curves
1083 were analysed with a Gehan-Breslow-Wilcoxon test (**$p < 0.01$, ***$p < 0.001$). **f**,

1084 Immunoblot analysis of PK-resistant Prp^{Sc} from the striatum, cortex, hippocampus and
1085 cerebellum of DTA^{M4*} and WT^{M4*} mice inoculated with NBH or RML-prion. Evaluated
1086 samples were collected at terminal stages of prion diseased mice with equivalent
1087 survival times. **g**, Quantification of Prp^{Sc} shows accumulation of the PK-resistant protein
1088 in all evaluated brain regions from diseased animals. Ablation of M_4^+ astrocytes
1089 significantly reduces the deposition of Prp^{Sc} in the cerebellum. Graph represents means
1090 ± SEM of Prp^{Sc} levels relative to α-tubulin expression (n = 4-6) expressed as a
1091 percentage of the values obtained for RML-prion diseased wild-type mice (WT^{M4*}).
1092 Statistical significance was calculated by two-way ANOVA followed by Tukey's post-hoc
1093 test (*$p < 0.05$, ***$p < 0.001$).

Fig. 1

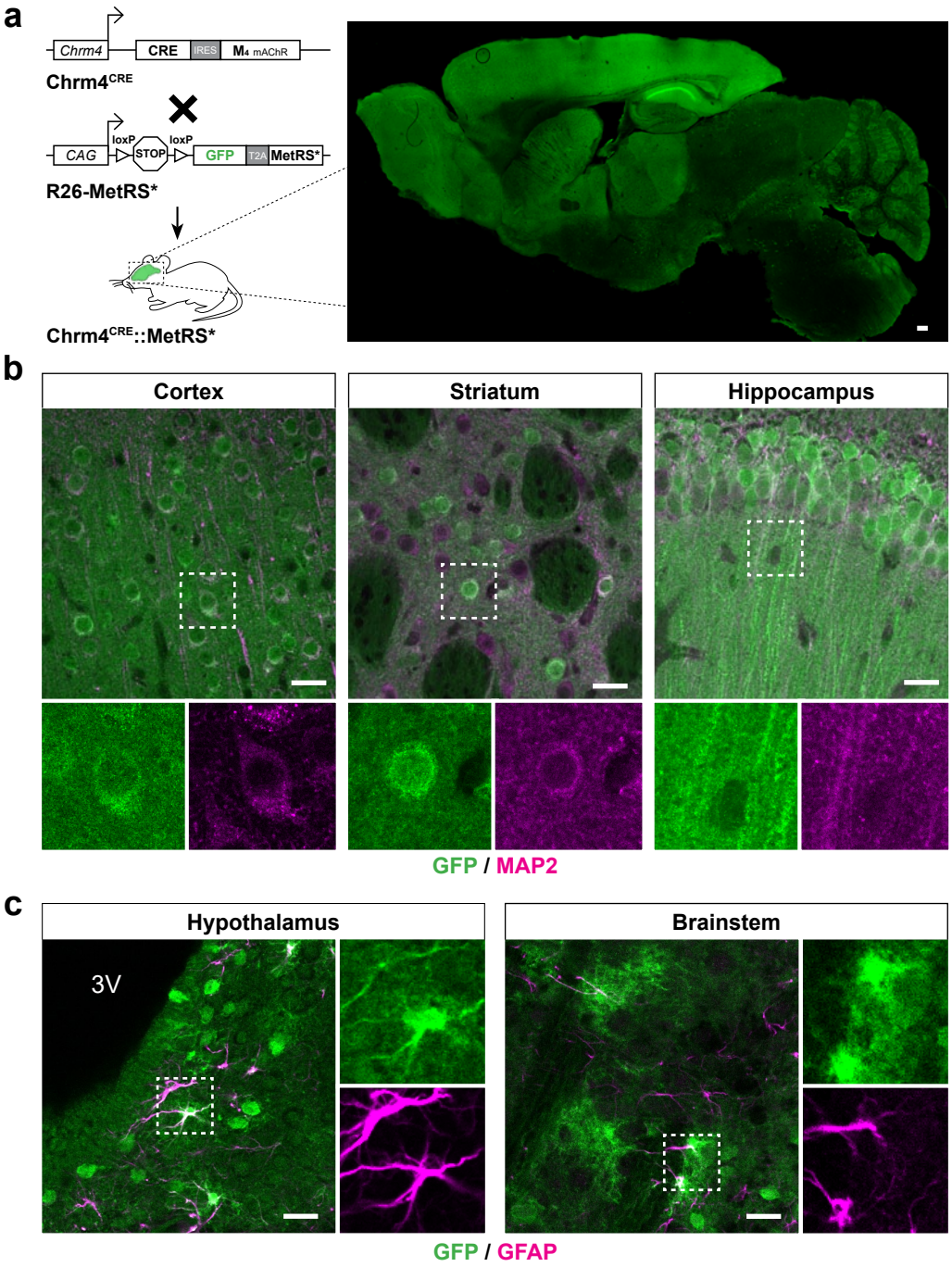
a
Chrm4
CRE
IRES
M4 mAChR
Chrm4CRE
CAG
loxP
STOP
loxP
GFP
T2A
MetRS*
R26-MetRS*
Chrm4CRE::MetRS*
b
Cortex
Striatum
Hippocampus
GFP / MAP2
c
Hypothalamus
3V
Brainstem
GFP / GFAP

Fig. 2

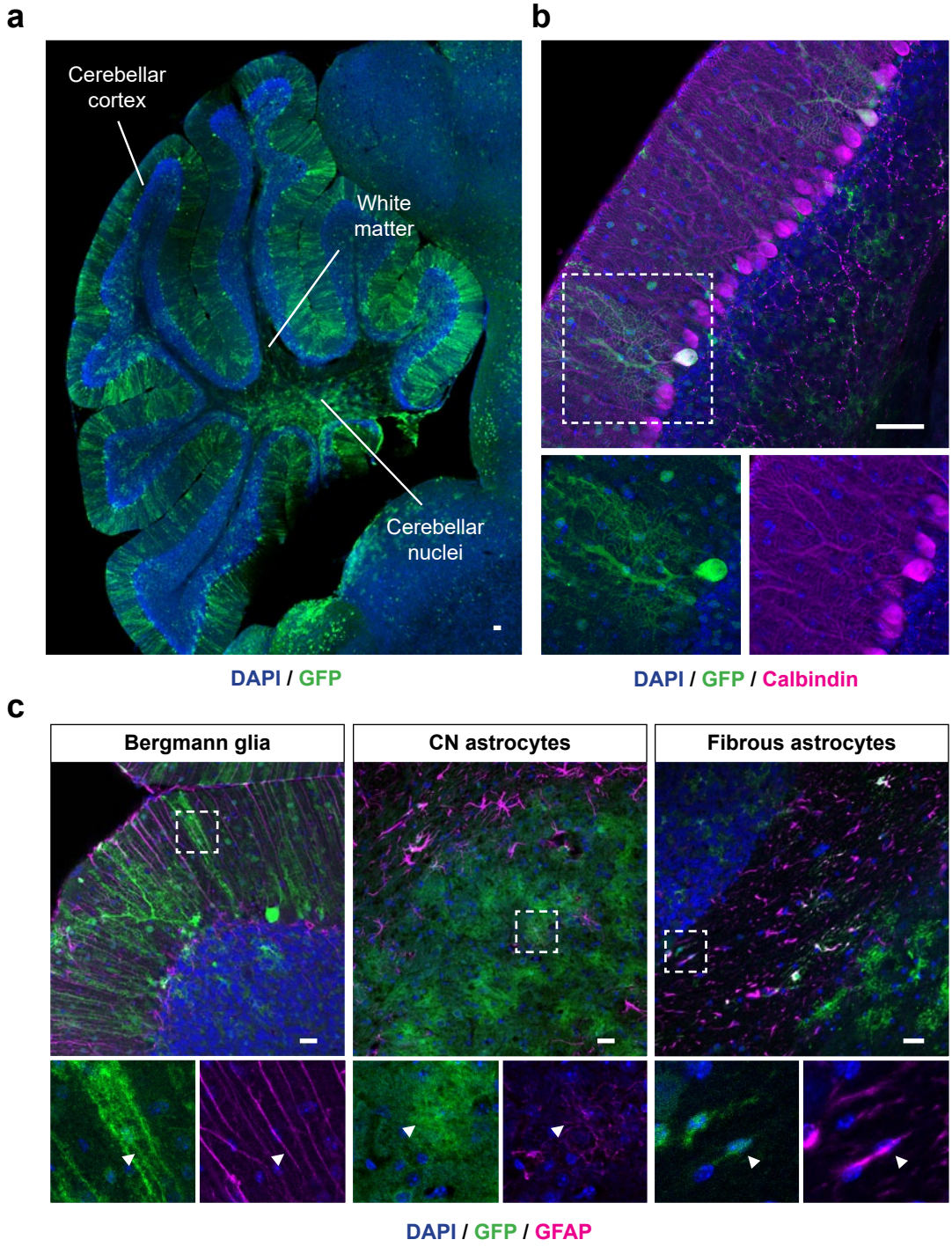
a
Cerebellar cortex
White matter
Cerebellar nuclei
DAPI / GFP
b
DAPI / GFP / Calbindin
c
Bergmann glia
CN astrocytes
Fibrous astrocytes
DAPI / GFP / GFAP

Fig. 3

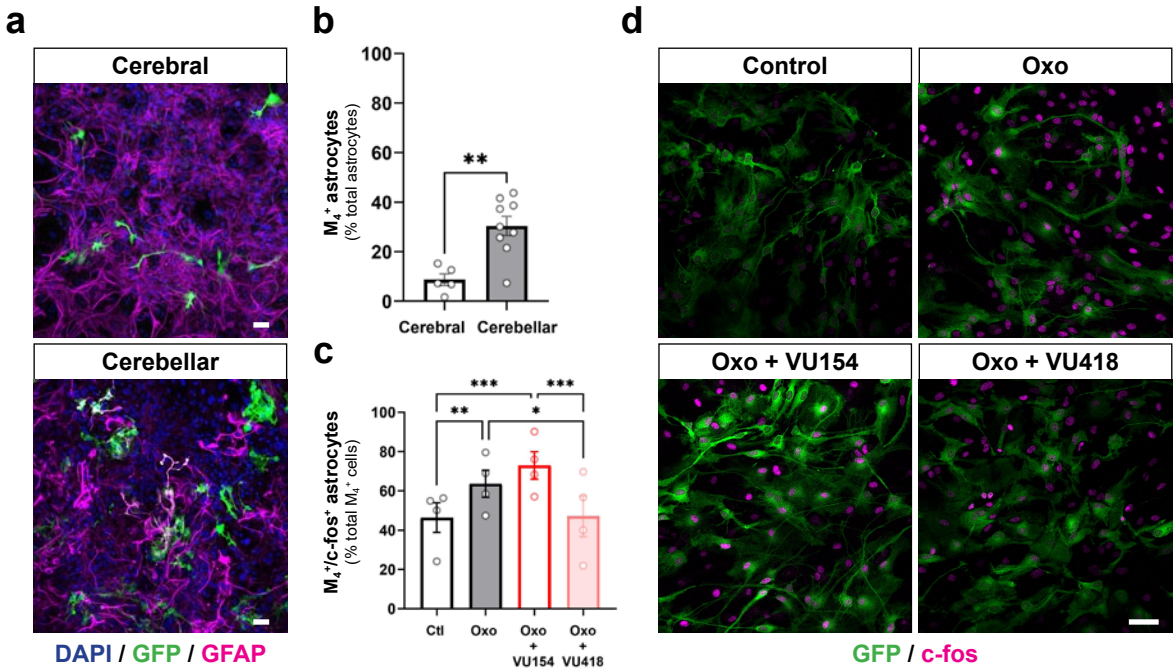
a
Cerebral
Cerebellar
DAPI / GFP / GFAP
b
M4+ astrocytes (% total astrocytes)
100
80
60
40
20
0
**
Cerebral
Cerebellar
c
M4+/c-fos+ astrocytes (% total M4+ cells)
***
**
*
***
Ctl
Oxo
Oxo + VU154
Oxo + VU418
d
Control
Oxo
Oxo + VU154
Oxo + VU418
GFP / c-fos

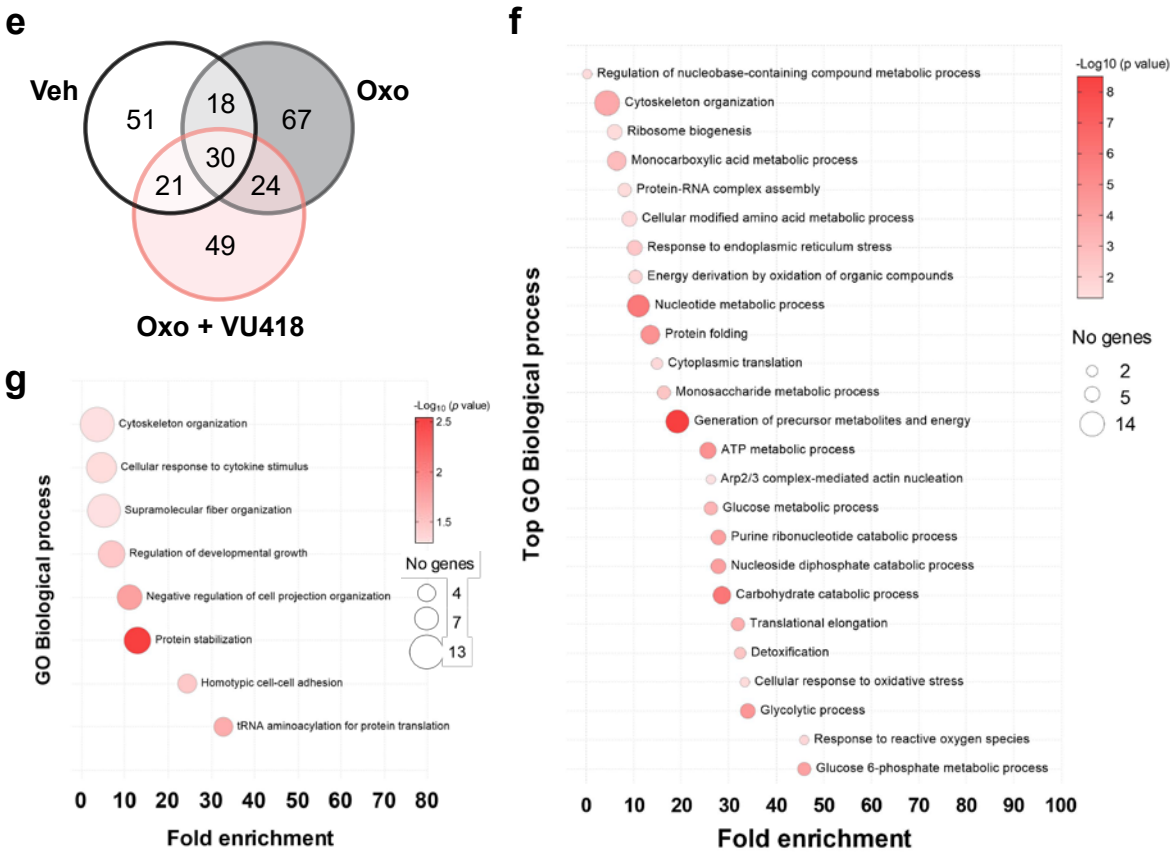
e
Veh
Oxo
Oxo + VU418
51
18
67
30
21
24
49
f
Top GO Biological process
Regulation of nucleobase-containing compound metabolic process
Cytoskeleton organization
Ribosome biogenesis
Monocarboxylic acid metabolic process
Protein-RNA complex assembly
Cellular modified amino acid metabolic process
Response to endoplasmic reticulum stress
Energy derivation by oxidation of organic compounds
Nucleotide metabolic process
Protein folding
Cytoplasmic translation
Monosaccharide metabolic process
Generation of precursor metabolites and energy
ATP metabolic process
Arp2/3 complex-mediated actin nucleation
Glucose metabolic process
Purine ribonucleotide catabolic process
Nucleoside diphosphate catabolic process
Carbohydrate catabolic process
Translational elongation
Detoxification
Cellular response to oxidative stress
Glycolytic process
Response to reactive oxygen species
Glucose 6-phosphate metabolic process
-Log10 (p value)
No genes
2
5
14
0 10 20 30 40 50 60 70 80 90 100
Fold enrichment
g
GO Biological process
Cytoskeleton organization
Cellular response to cytokine stimulus
Supramolecular fiber organization
Regulation of developmental growth
Negative regulation of cell projection organization
Protein stabilization
Homotypic cell-cell adhesion
tRNA aminoacylation for protein translation
-Log10 (p value)
No genes
4
7
13
0 10 20 30 40 50 60 70 80
Fold enrichment

Fig. 4

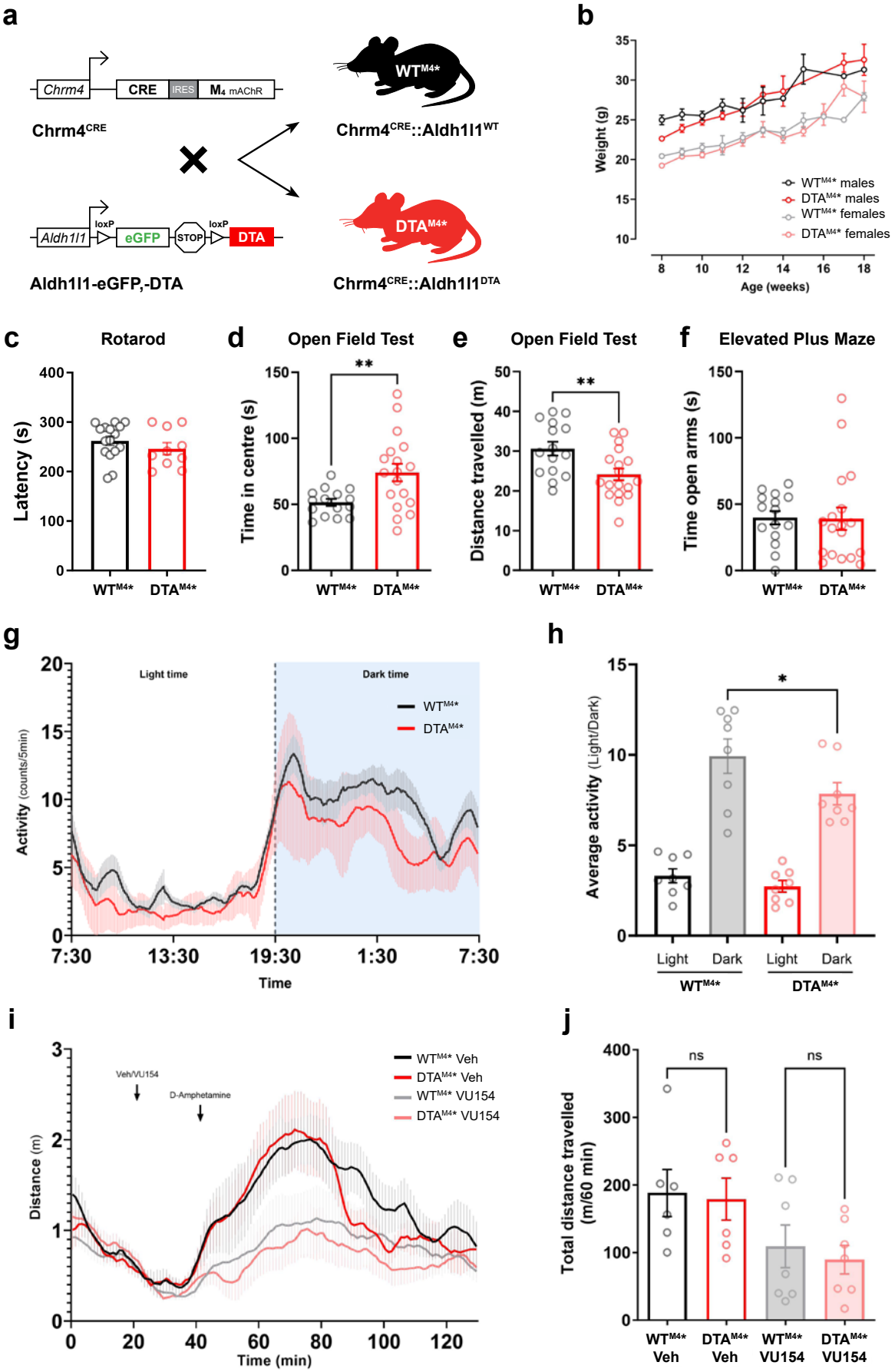
a
Chrm4
CRE
IRES
M4 mAChR
Chrm4CRE
WTM4*
Chrm4CRE::Aldh1l1WT
Aldh1l1
loxP
eGFP
STOP
loxP
DTA
Aldh1l1-eGFP,-DTA
DTAM4*
Chrm4CRE::Aldh1l1DTA
b
Weight (g)
Age (weeks)
WTM4* males
DTAM4* males
WTM4* females
DTAM4* females
c
Rotarod
Latency (s)
WTM4*
DTAM4*
d
Open Field Test
Time in centre (s)
**
e
Open Field Test
Distance travelled (m)
**
f
Elevated Plus Maze
Time open arms (s)
g
Light time
Dark time
Activity (counts/5min)
Time
h
Average activity (Light/Dark)
*
Light
Dark
i
Veh/VU154
D-Amphetamine
Distance (m)
Time (min)
WTM4* Veh
DTAM4* Veh
WTM4* VU154
DTAM4* VU154
j
Total distance travelled (m/60 min)
ns
ns
WTM4* Veh
DTAM4* Veh
WTM4* VU154
DTAM4* VU154

Fig. 5

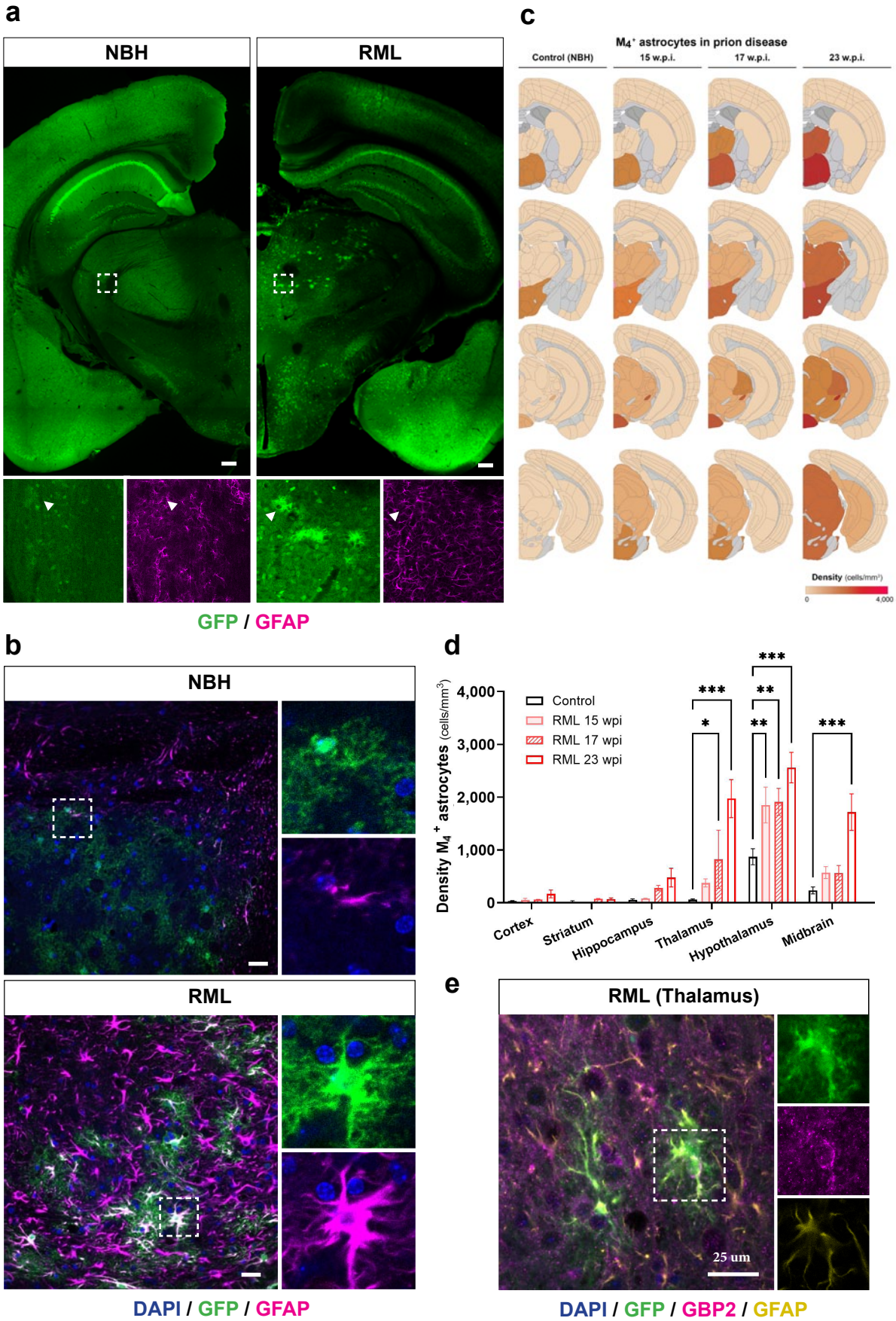
a
NBH
RML
GFP / GFAP
c
M4+ astrocytes in prion disease
Control (NBH)
15 w.p.i.
17 w.p.i.
23 w.p.i.
Density (cells/mm³)
0
4,000
b
NBH
RML
DAPI / GFP / GFAP
d
Density M4+ astrocytes (cells/mm3)
4,000
3,000
2,000
1,000
0
Control
RML 15 wpi
RML 17 wpi
RML 23 wpi
Cortex
Striatum
Hippocampus
Thalamus
Hypothalamus
Midbrain
e
RML (Thalamus)
25 um
DAPI / GFP / GBP2 / GFAP

Fig. 6

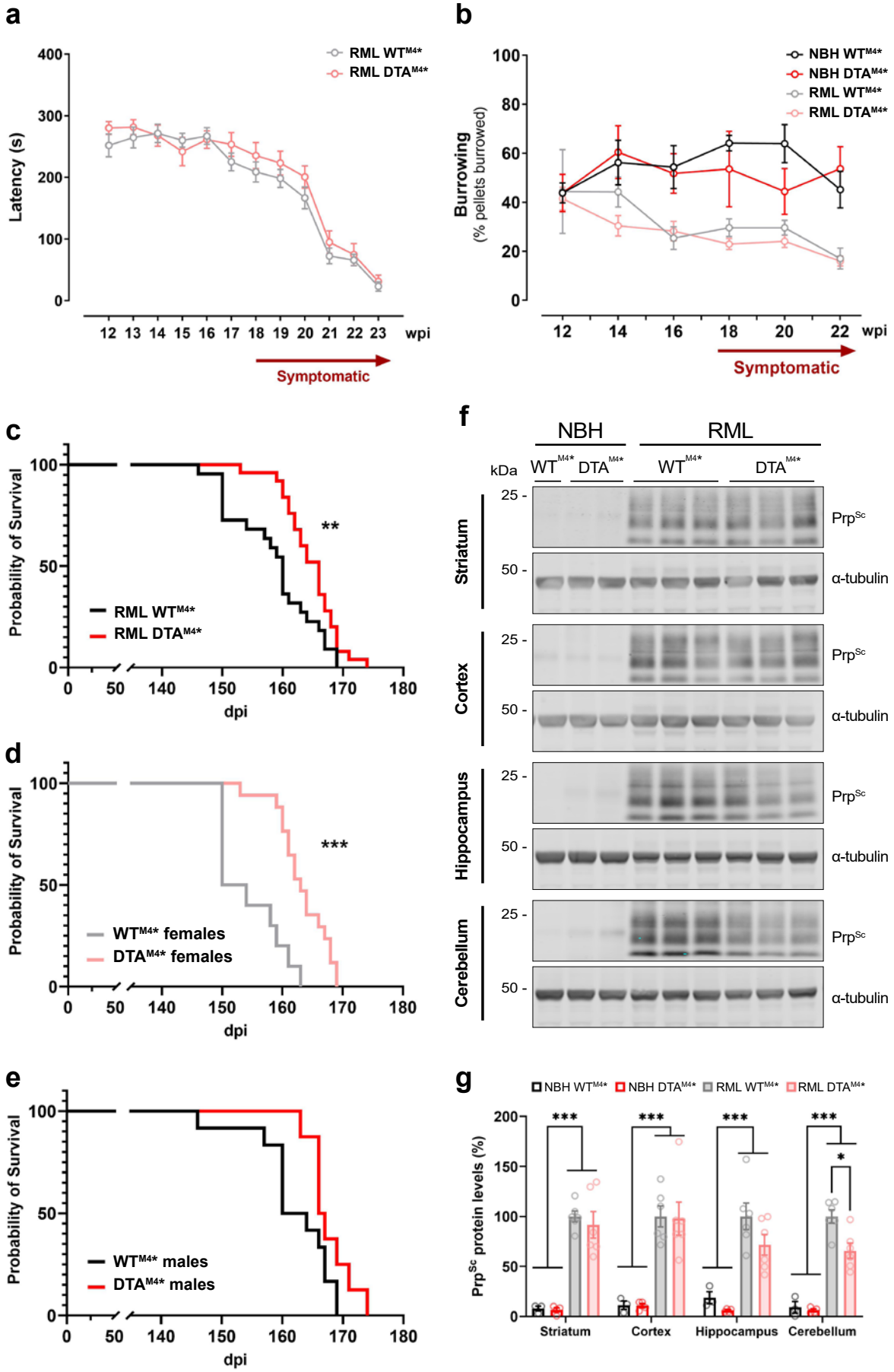
a
Latency (s)
RML WT^M4*
RML DTA^M4*
wpi
Symptomatic
b
Burrowing (% pellets burrowed)
NBH WT^M4*
NBH DTA^M4*
RML WT^M4*
RML DTA^M4*
wpi
Symptomatic
c
Probability of Survival
RML WT^M4*
RML DTA^M4*
**
dpi
d
Probability of Survival
WT^M4* females
DTA^M4* females
***
dpi
e
Probability of Survival
WT^M4* males
DTA^M4* males
dpi
f
NBH
RML
kDa
WT^M4*
DTA^M4*
WT^M4*
DTA^M4*
Striatum
Cortex
Hippocampus
Cerebellum
Prp^Sc
α-tubulin
g
NBH WT^M4*
NBH DTA^M4*
RML WT^M4*
RML DTA^M4*
Prp^Sc protein levels (%)
Striatum
Cortex
Hippocampus
Cerebellum